

REPORT DOCUMENTATION PAGE

AFRL-SR-BL-TR-01-

Public reporting burden for this collection of information is estimated to average 1 hour per response, including the time for reviewing instructions, searching existing data sources, gathering and maintaining the data needed, and completing and reviewing this collection of information. Send comments regarding this burden estimate to Washington Headquarters Services, Directorate for Information Operations and Reports, 1215 Jefferson Davis Highway, Suite 1202, Arlington, VA 22202-4302, and to the Office of Management and Budget, Paperwork Reduction Project (0704-0188), Washington, DC 20503.

CGHJ

aintaining
tions for
2002-4302, and to the Office of

1. AGENCY USE ONLY (Leave blank)			2. REPORT DATE Final Technical Report 1 Dec 98 - 30 Nov 99		3. REPORT TYPE AND DATES COVERED Final Technical Report 1 Dec 98 - 30 Nov 99		
4. TITLE AND SUBTITLE A Comprehensive Investigation of Advanced Range Telemetry			5. FUNDING NUMBERS F49620-99-1-0056				
6. AUTHOR(S) Michael Rice							
7. PERFORMING ORGANIZATION NAME(S) AND ADDRESS(ES) Department of Electrical & Computer Engineering 459 Clyde Building Brigham Young University Provo, UT 84602					8. PERFORMING ORGANIZATION REPORT NUMBER N/A		
9. SPONSORING / MONITORING AGENCY NAME(S) AND ADDRESS(ES) AFOSR/NM Attn: Dr. Len Sakell 110 Duncan Ave Suite B 115 Bolling AFB, DC 20332-8050					MONITORING 20011203 171		
11. SUPPLEMENTARY NOTES None			AIR FORCE OFFICE OF SCIENTIFIC RESEARCH (AFOSR) NOTICE OF TRANSMISSION DRAFT THIS TECHNICAL REPORT HAS BEEN REVIEWED AND IS APPROVED FOR PUBLIC RELEASE LAW AFR 190-12. DISTRIBUTION IS UNLIMTED N/A				
12a. DISTRIBUTION / AVAILABILITY STATEMENT None Approved for public release, distribution unlimited			12b. DISTRIBUTION CODE N/A				
13. ABSTRACT (Maximum 200 Words) Data from ARTM channel sounding flights has been analyzed. A three-path model consisting of a line-of-sight path and two reflected paths adequately captures all the essential multipath features of the aeronautical telemetry channel. The amplitudes and delays of the multipath reflections are the same for L-Band and S-Band. Antenna diameter does have an effect: larger antenna diameters result in lower amplitudes on the short-delay multipath reflection. Flight 18 data demonstrated a great deal of spatial diversity for two antennas with 40-foot vertical separation. An analysis of the effects of multipath on the bit error rate for BPSK matches measurements taken during the channel sounding flights. The dynamic behavior of the channel is measured using the Doppler power spectrum which have a bandwidth of about 10 Hz. Thus the coherence time of the channel is approximately 100 ms.							
14. SUBJECT TERMS Channel sounding, multipath fading, aeronautical telemetry					15. NUMBER OF PAGES 81		
					16. PRICE CODE		
17. SECURITY CLASSIFICATION OF REPORT None F49620-99-1-		18. SECURITY CLASSIFICATION OF THIS PAGE None		19. SECURITY CLASSIFICATION OF ABSTRACT None		20. LIMITATION OF ABSTRACT None	

TABLE OF CONTENTS

1	Executive Summary.....	2
2	Effects of carrier frequency and antenna diameter on frequency selective multipath fading ..	4
2.1	Antenna Gain and Beamwidth Characteristics	4
2.2	Analysis Procedure	6
2.3	Results.....	6
3	Bit Error Performance Analysis of BPSK in the Presence of Multipath Fading.....	13
3.1	Simulation of Theoretic Results.....	16
3.2	ARTM Channel Sounding Results	19
4	Dynamic behavior of Multipath Interference in ARTM Channel Sounding Data	20
4.1	Dynamics of the Channel Model	21
4.2	Dynamics of the Channel Sounding Data.....	24
4.3	Doppler Bandwidth Characterization of Channel Dynamics.....	25
5	Parametric Estimation of the Scattering Function for ARTM Channel Sounding Data	27
5.1	Mathematical Development and Modeling Assumptions.....	28
5.2	Estimating the Scattering Function.....	29
5.3	A Comparison of Scattering Function Estimates for Varied Channel Behaviors.....	34
5.4	Results.....	36
6	References	37

1 EXECUTIVE SUMMARY

This report summarizes the results of the work on channel characterization for the Advanced Range Telemetry (ARTM) program. Data collected from channel sounding flights was used to determine characteristics of multipath reflections for typical environments. In previous work, it was shown that two multipath reflections are sufficient to characterize the multipath interference experienced in aeronautical telemetering applications. An investigation of the dependence of the path gains and delays as a function of carrier frequency and receive antenna diameter showed that the effects of carrier frequencies (L-Band and S-Band) on multipath fading characteristics were statistically similar in terms of reflection magnitude and delay. However, the results from the effects of antenna diameter show that there was a greater attenuation of the first multipath reflection from the larger antenna due to a narrow main lobe and small side lobe characteristics of the antenna gain pattern. Also, data from Flight 18 revealed that vertical diversity of antenna position results in different fading event times for transmitted signals arriving at each of the receive antennas.

The effects of the amplitudes, phases, and delays of the multipath reflections on the bit error rate performance of BPSK was also studied. Analytical results were derived which agreed with the bit error rate tests performed in conjunction with the channel sounding flights.

The dynamic channel model is based on the scattering function and Doppler spectrum. Early ARTM channel sounding runs did not have a high enough spatial sampling rate to produce unaliased estimates of the Doppler spectrum. Flight 18 was taken with a higher spatial sampling rate. We showed with both our channel model and examples of fades in our data how the multipath fades evolve over time in the frequency domain. They were shown to move in several different ways. They may grow and diminish in magnitude, or they may drift in frequency. This may be caused by several reasons, but one plausible explanation would be that these are changing due to a change in the differential path length between the LOS signal and the multipath reflection. The rate of change of the fade events compared with that of the differential path lengths would support this assumption. Many reflections may also be moving in and out of the main lobe of the receiving antenna, which would also cause the fades to grow or diminish in magnitude. The coherence time, or the amount of time the channel can be viewed as unchanging, was found to be the 100 ms for the data sets examined. Thus, the multipath fade events could be viewed as an unchanging event for no longer than 100 ms thus implying that adaptive multipath mitigation techniques must have an adaptation bandwidth of 10 Hz.

Finally, we demonstrated that using the channel model parameters to estimate the correlation functions that describe the scattering function produced Doppler power spectra that were a good match to the Doppler power spectra derived directly from the data samples.

One thesis and four conference papers resulted from this work. The references are

- [1] David Landon, *An Analysis of Dynamic Behavior of the Aeronautical Telemetry Channel*. Thesis, Brigham Young University, 1999.

- [2] Adam Davis and Michael Rice, "Dynamic Behavior of Multipath Interference in ARTM Channel Sounding Data," in *Proceeding of the International Telemetering Conference*, San Diego, CA, October 2000.
- [3] Vladimir I. Paje and Michael Rice, "The Effects of Carrier Frequency and Antenna Diameter on Frequency Selective Multipath Fading," in *Proceeding of the International Telemetering Conference*, San Diego, CA, October 2000.
- [4] David E. de Gaston and Michael Rice, "Bit Error Performance Analysis fo BPSK in the Presence of Multipath Fading," in *Proceeding of the International Telemetering Conference*, San Diego, CA, October 2000.
- [5] David Landon and Michael Rice, "Parametric Estimation of the Scattering Function for ARTM Channel Sounding Data," in *Proceeding of the International Telemetering Conference*, San Diego, CA, October 2000.

2 EFFECTS OF CARRIER FREQUENCY AND ANTENNA DIAMETER ON FREQUENCY SELECTIVE MULTIPATH FADING

The initial results from two ARTM channel sounding flights at Edwards AFB (December 1998 and February 1999) have shown that the telemetry channel can be modeled as a linear time-invariant system with one line of site component and two reflective components [1]. The impulse response of the channel is given as

$$h(t) = \delta(t) + \Gamma_1 e^{j\gamma_1} \delta(t - \tau_1) + \Gamma_2 e^{j\gamma_2} \delta(t - \tau_2) \quad (2.1)$$

where Γ_i ($i = 1, 2$) represents the magnitude of the first and second reflection with respect to the line-of-sight signal, τ_i ($i = 1, 2$) represents the delay of the respective reflections, and γ_i ($i = 1, 2$) represents a component of the phase shift. In this paper, we are only interested in the Γ and τ parameters. Frequency domain techniques were used to characterize the data by computing the power spectral densities of the transmitted and received signals, denoted by $S_x(f)$ and $S_y(f)$ respectively, and using the following relationship to determine the squared magnitude of the channel transfer function:

$$|\hat{H}(f)|^2 = \frac{S_y(f)}{S_x(f)} \quad (2.2)$$

The channel parameters then can be determined from the channel transfer function by the following equation (based on a two ray model):

$$|\hat{H}(f)|^2 = 1 + \Gamma^2 + 2\Gamma \cos(2\pi f \tau - \gamma) \quad (2.3)$$

A model with only two reflection components shows good results with the data available from the ARTM flights at Edwards AFB.

2.1 Antenna Gain and Beamwidth Characteristics

The parabolic reflectors used as the receive antenna for the channel sounding flights at Edwards AFB have a circular symmetric gain pattern with the maximum gain, g , and half-power beamwidth, ϕ_b , given as the following [2]:

$$g = \left(\frac{\pi d}{\lambda} \right)^2 \quad (2.4)$$

$$\phi_b = \frac{1.02\lambda}{d} \quad (2.5)$$

where λ is the wavelength of the modulated carrier frequency and d is the diameter of the reflector. The gain pattern is given as [3]

$$G(\theta_b) = g \left(\frac{2J_1(u)}{u} \right)^2 \quad (2.6)$$

where $J_1(\bullet)$ is the Bessel function of the first kind, and

$$u = \frac{\pi d \sin(\theta_b)}{\lambda} \quad (2.7)$$

where θ_b is the angle off boresight. Figure 2.1 shows the antenna gain pattern for an 8-foot parabolic reflector operating at L-Band (1500MHz).

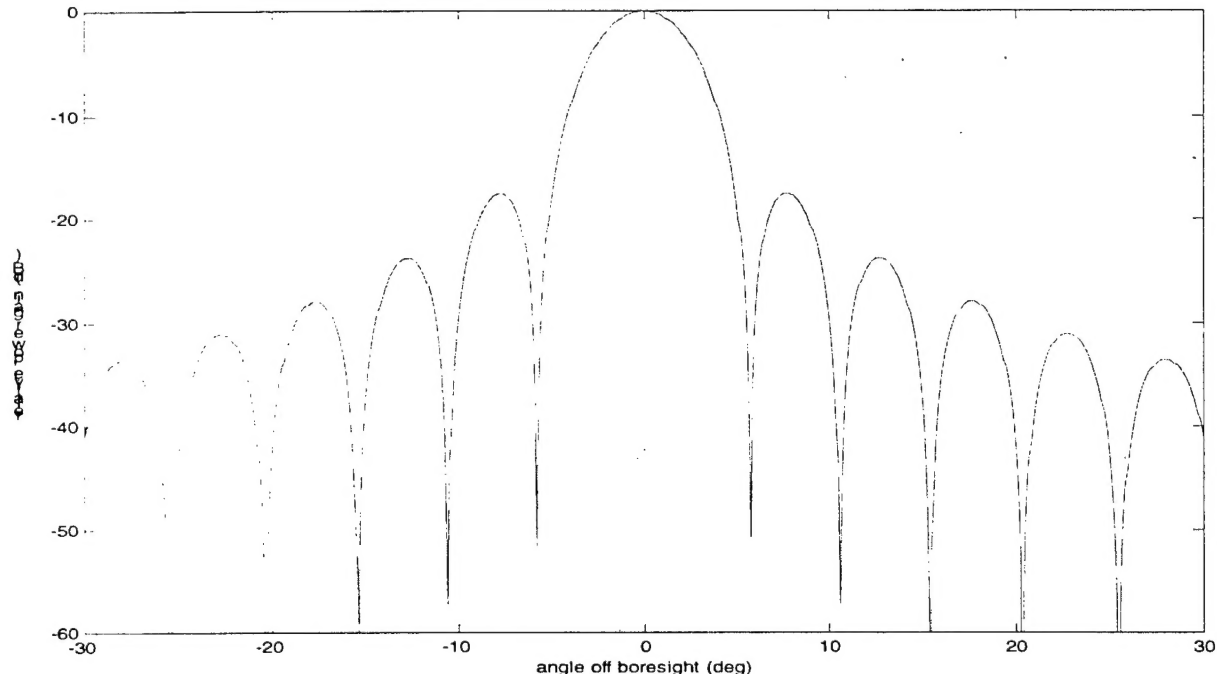


Figure 2.1: Antenna gain pattern for an 8 foot parabolic reflector at L-band (1500MHz)

Equations (2.4) and (2.5) show that the gain is proportional to the square of the antenna diameter and carrier frequency, and the half-power beamwidth varies inversely to the diameter and frequency [2]. With a constant carrier frequency, the receive radiation pattern for a small diameter antenna is characterized by a wider main lobe with high sidelobes. A larger diameter antenna exhibits a larger narrow main lobe with low side lobes. A larger diameter antenna would attenuate more of the short delay reflections since the angle of incident is high. We would expect a stronger short delay reflection from the small diameter antenna.

2.2 Analysis Procedure

Data used in this paper was obtained from the flight data gathered at Edwards AFB. Table 1 lists the different configurations of carrier frequency and antenna size used for each flight, plus the flight path. These data sets allowed us to compare multipath fading (in terms of Γ and τ) as a function of frequency band and antenna size.

Flight Number	Frequency Band	Antenna Size(s)	Location
10 (10 Dec 98)	L	8'	Cord's Rd 5,000 ft Black Mnt 5,000 ft & 10,000 ft
11 (16 Feb 99)	S	15'	Cord's Rd 5,000 ft
12 (22 Feb 99)	S	8', 8'	Cord's Rd 5,000 ft Black Mnt 5,000 ft & 10,000 ft
18 (28 Jul 99)	L	8', 4'	Cord's Rd 5,000 ft Black Mnt 5,000 ft & 10,000 ft

Table 2.1: Technical specification summary the flights at Edwards AFB

To compare the effects of carrier frequency on multipath fading, we used data sets from Flight 10 (L-band) and Flight 12 (S-band). The antenna size on both flights is 8 feet. To compare the effects of antenna size on multipath fading, we used data sets from Flight 11 (15-foot dish) and Flight 12 (8-foot dish). Both flights use the S-band carrier frequency. Flight 18 data provided a unique and more precise comparison of antenna size to multipath fading since both antennas were concurrently receiving data under the same environmental conditions.

2.3 Results

For the first results, we compare the effects of carrier frequency on multipath fading using data from Flights 10 and 12, noting that the antenna diameter is 8 feet in both flights. Figures 2.2 and 2.3 show a summary of the 3-ray modeling results of the Cord's Road run for Flights 10 and 12, respectively. The plots in the left column are based on the parameters of the first reflection ($\Gamma_1 \tau_1$), and the right column plots are based on the second reflection parameters reflection ($\Gamma_2 \tau_2$). The top graphs show a plot of the magnitude and delay for each of the respective reflections. The middle and bottom graphs show a histogram of the delays and magnitudes for the first and second multipath reflections, with the mean values noted. From the plots, we observe that the magnitude and delays for the two multipath reflections are similar in both flights, suggesting that the multipath characteristics are statistically the same at L and S band.

Figures 2.4 and 2.5 are the same as Figures 2.2 and 2.3 except that the data set used was the Black Mountain Run at 5000 feet and the plot of the magnitude versus delay for each of the respective reflections were omitted. These results also show that L and S band carrier frequencies have similar multipath characteristics.

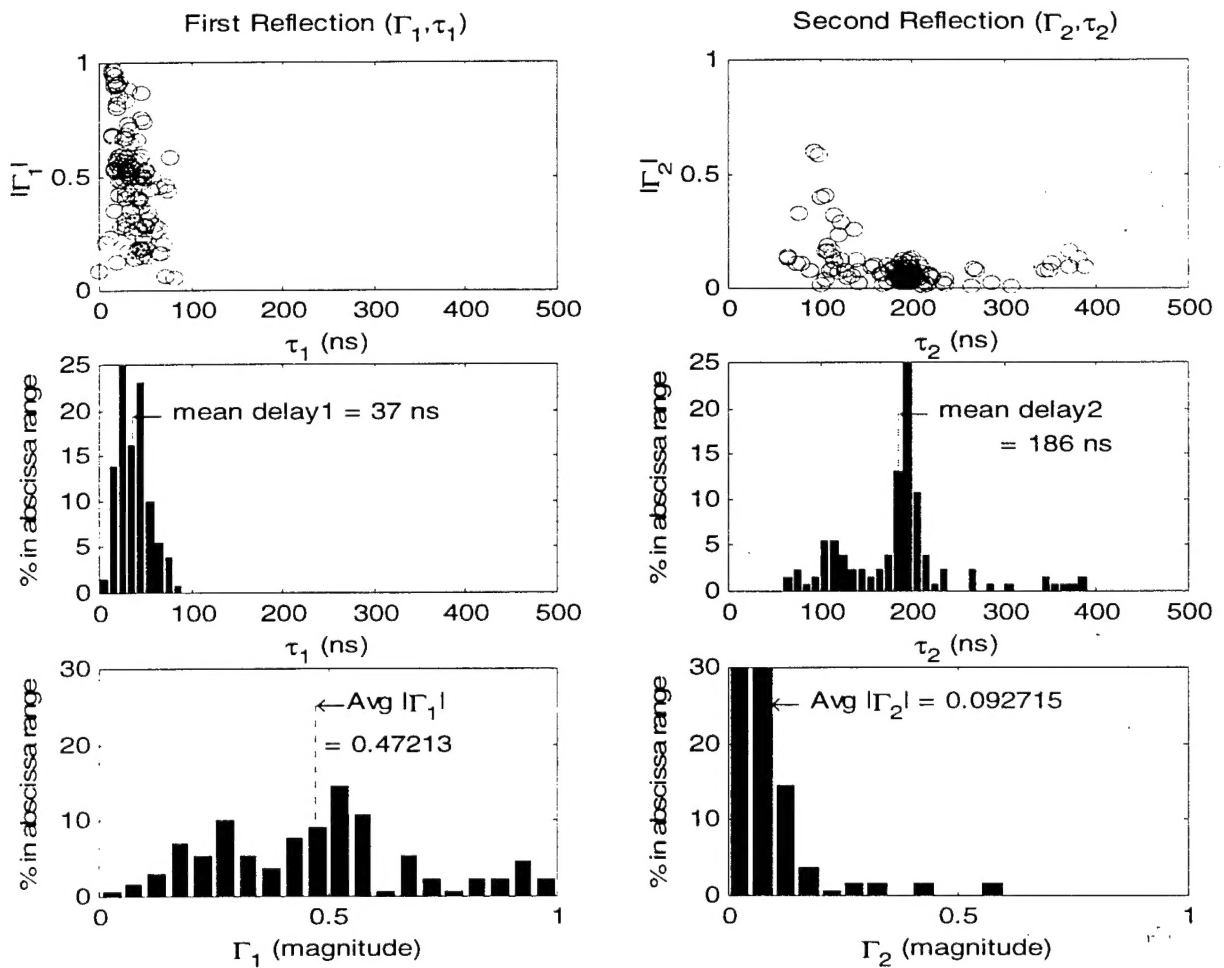


Figure 2.2: Parameter summaries of the 3-ray model for the Cord's Road Run (ARTM Flight 10) at Edwards AFB with an aircraft at an altitude of 5,000 feet.

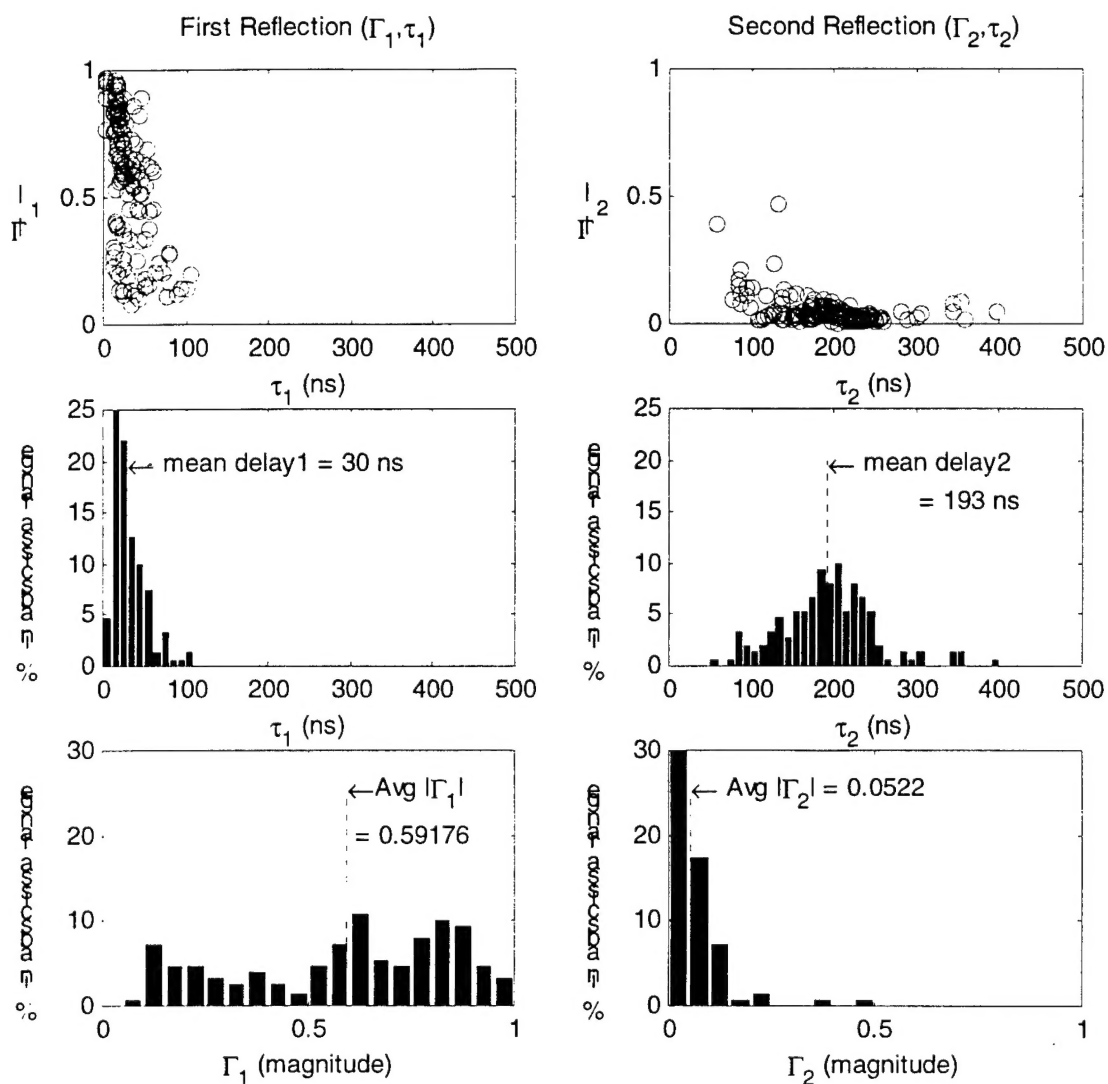


Figure 2.3: Parameter summaries of the 3-ray model for the Cord's Road Run (ARTM Flight 12) at Edwards AFB with an aircraft at an altitude of 5,000 feet.

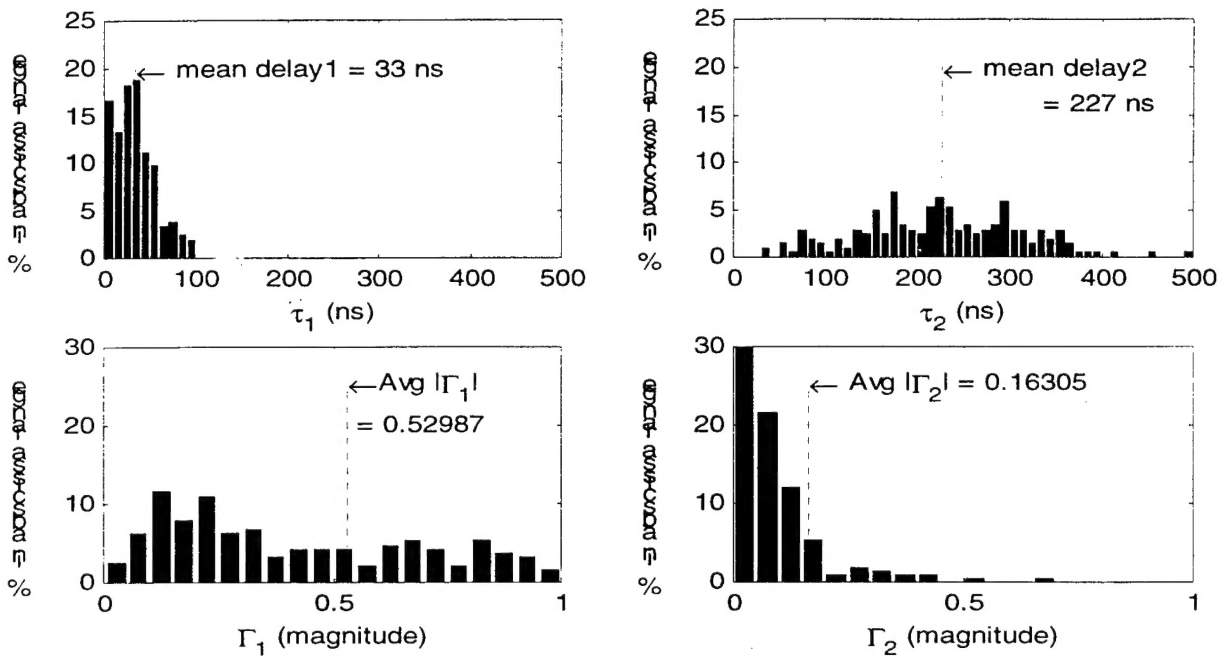


Figure 2.4: Parameter summaries of the 3-ray model for the Black Mountain Run (ARTM Flight 10) at Edwards AFB with an aircraft at an altitude of 5,000 feet.

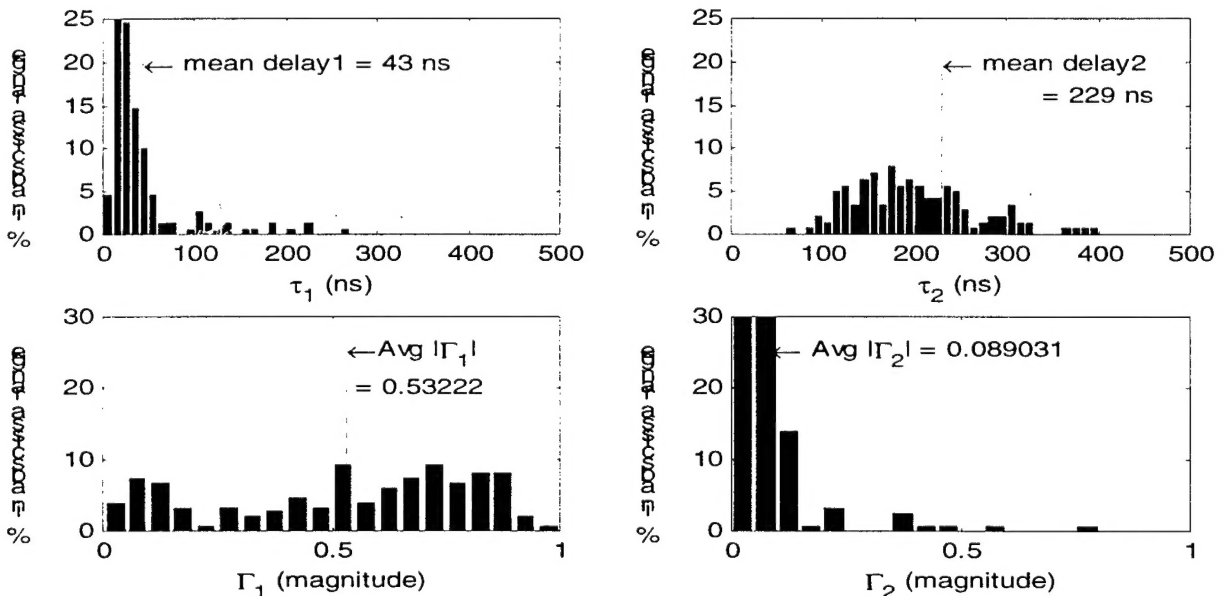


Figure 2.5: Parameter summaries of the 3-ray model for the Black Mountain Run (ARTM Flight 12) at Edwards AFB with an aircraft at an altitude of 5,000 feet.

In the next results, we compare the effects of antenna diameter on multipath fading using data from Flight 11 (15-foot antenna) and Flight 12 (8-foot antenna). The S-band carrier frequency is used in both flights. Figure 6 shows a summary of the 3-ray modeling results of the Cord's Road run for Flight 11. Comparing this plot with the Flight 12 Cord's Road run (Figure 2.3), we notice some subtle differences. The relative amplitude of the short delay reflections for Flight 12 is slightly higher than in Flight 11. The short delay reflections occur close to the antenna site where the angle of incident is high. This steep angle causes a higher attenuation in Flight 11 because of the narrow main lobe, low side lobe characteristics of a larger dish size. For the relative amplitude of the long delay reflections, no concrete conclusion can be made because the variance between the two flights may be due to non-controllable parameters (different flight days, varying flight paths, equipment calibration differences).

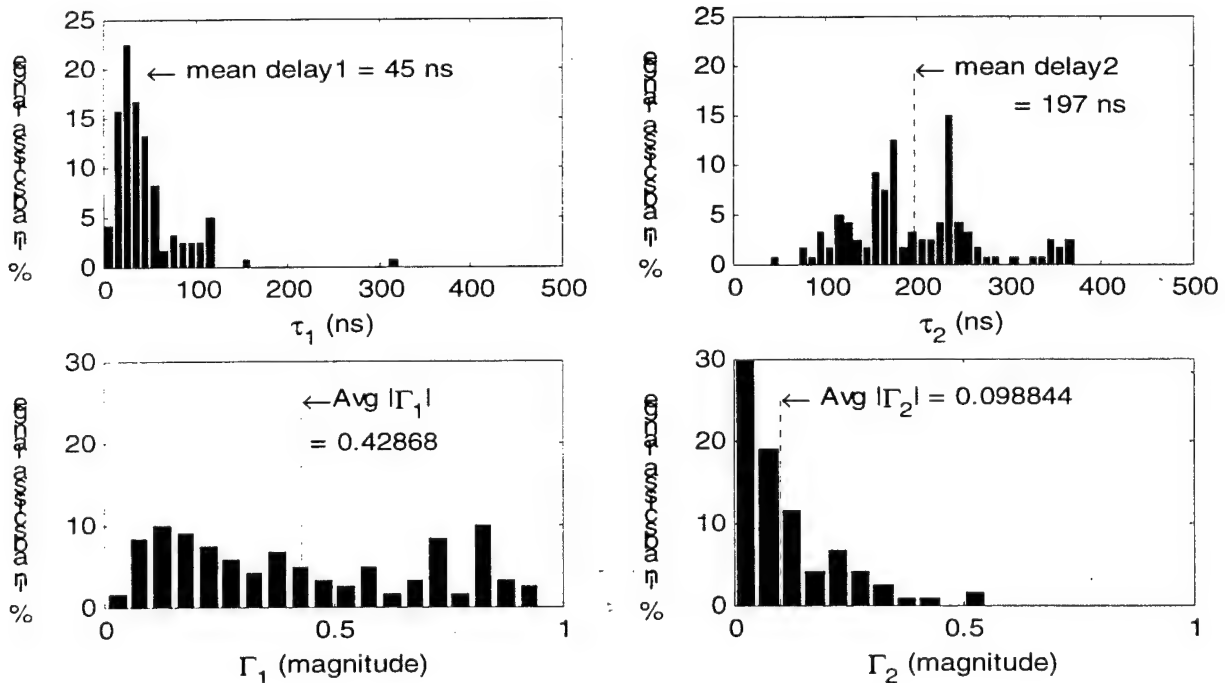


Figure 2.6: Parameter summaries of the 3-ray model for the Cord's Road Run (ARTM Flight 11) at Edwards AFB with an aircraft at an altitude of 5,000 feet.

We also compared the effects of antenna diameter on multipath fading using data from Flight 18. Figure 2.7 shows a summary of the 2-ray modeling results for one time stamp (200 samples from a 16 second segment) of the Black Mountain Run for Flight 18. The graphs in the left column are from Antenna 2 (8') and the right column graphs are from Antenna 3 (4'). These results show that the average magnitude of the reflection is slightly higher with the 8' antenna than with the 4' antenna (0.57 vs 0.48). Table 2.2 lists the average reflection magnitude for three time stamps from the two antennas of Flight 18. This data also shows that the reflection magnitude from the 8' antenna are higher than with the 4' antenna. While this may appear to be contradictory to the previous results, the difference is due to the vertical antenna diversity. The two receive antennas used in Flight 18 are positioned 150 feet apart horizontally and 40 feet vertically. It has been shown in other flight data that horizontally diversity does not lead to a

significant change in multipath fade events, but the vertical change does produce different fade events between the two antennas and thus we cannot just compare relative magnitudes alone.

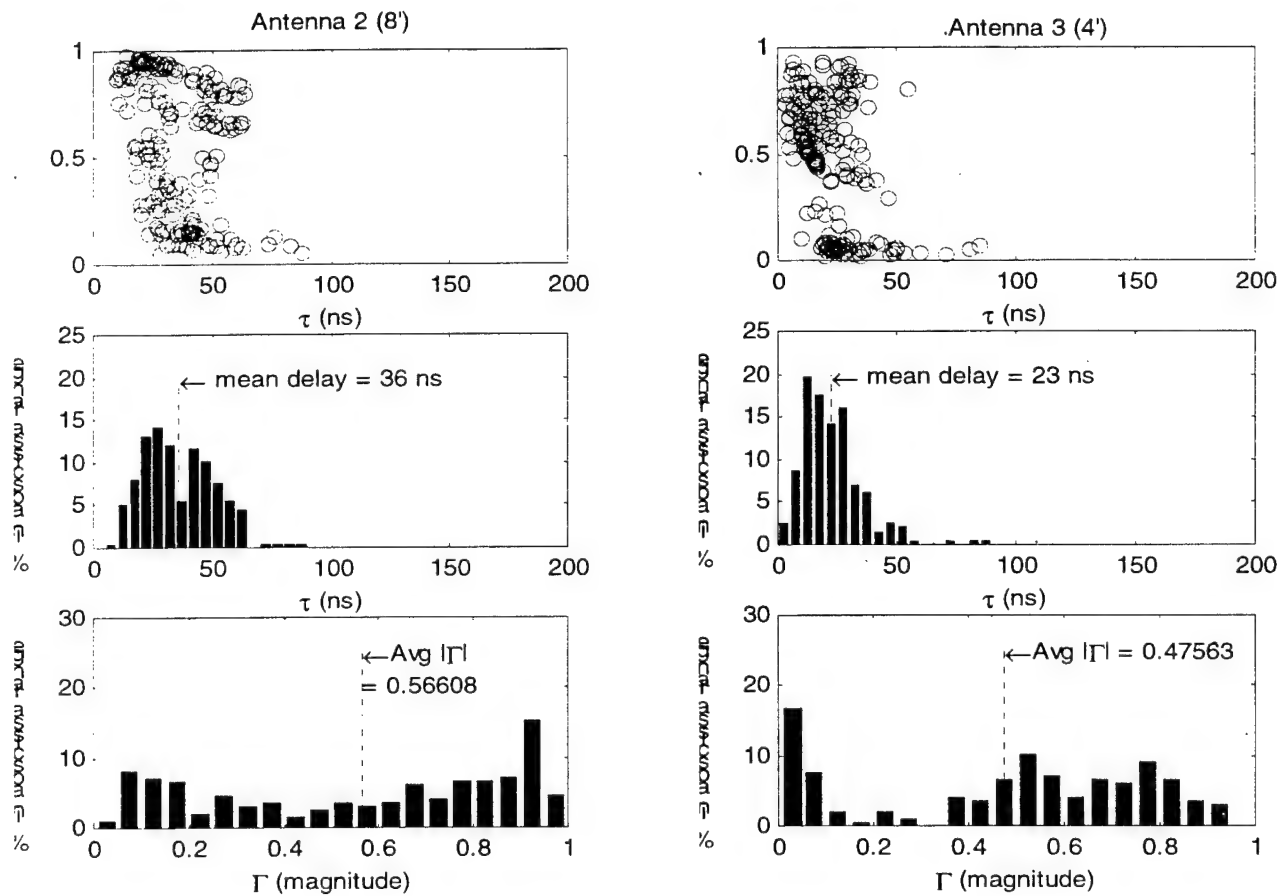


Figure 2.7: Parameter summaries of the 2-ray model for one time stamp (200 samples from a 16 second segment) for the Cord's Road Run (ARTM Flight 18) at Edwards AFB with an aircraft at an altitude of 5,000 feet.

Location	Antenna 2 (8')	Antenna 3 (4')
Black Mnt (W-E) 5,000ft	0.508	0.377
Black Mnt (E-W) 5,000ft	0.344	0.338
Cord's Road (E-W) 5,000ft	0.566	0.476

Table 2.2: List of average reflection magnitudes ($|\Gamma|$) for three different time stamps for ARTM Flight 18 at Edwards AFB.

Figures 2.8 and 2.9 show a plot of reflection magnitude versus time for both antennas in their respective time stamp of Flight 18. Clearly, the peak magnitudes, corresponding to deep fading events, appear at different times and is somewhat inverted to each other. These differing fade events show promising results that vertical antenna diversity may provide a positive mitigation technique to effectively minimize data loss when multipath fading occurs.

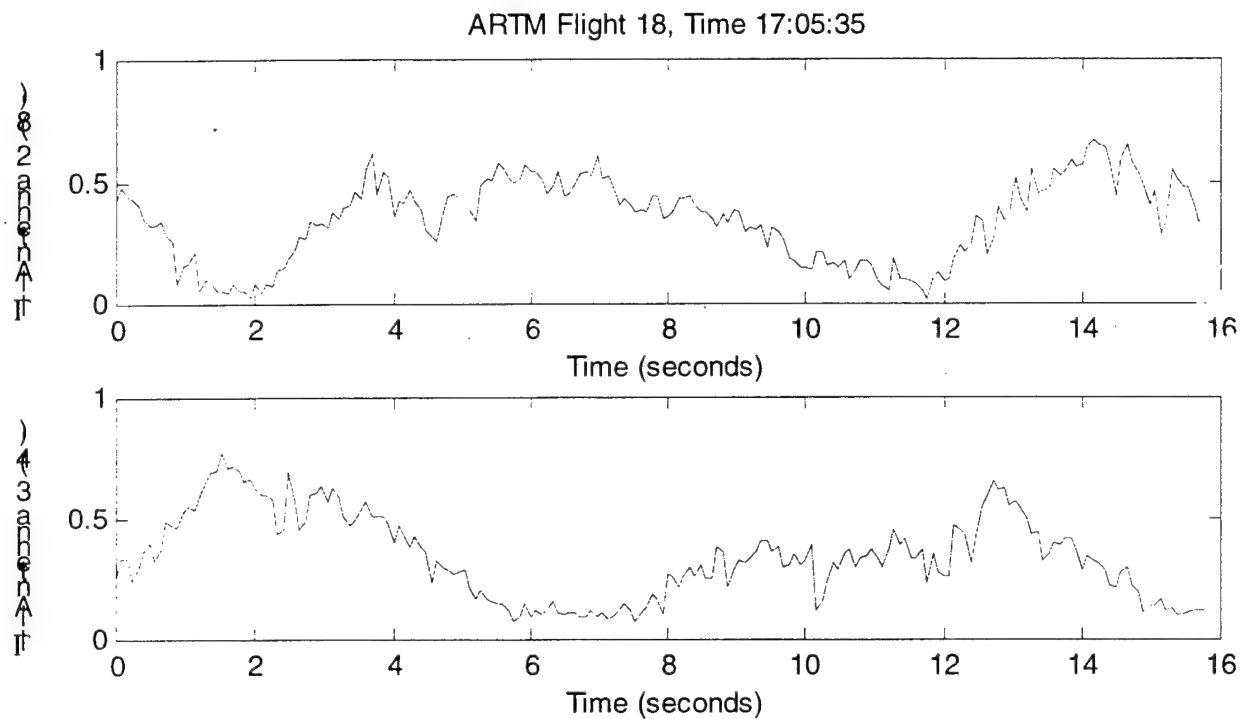


Figure 2.8: Plot of $|T|$ vs Time for Black Mountain Run (ARTM Flight 18, Time 17:05:35) at Edwards AFB with an aircraft at an altitude of 5,000 feet.

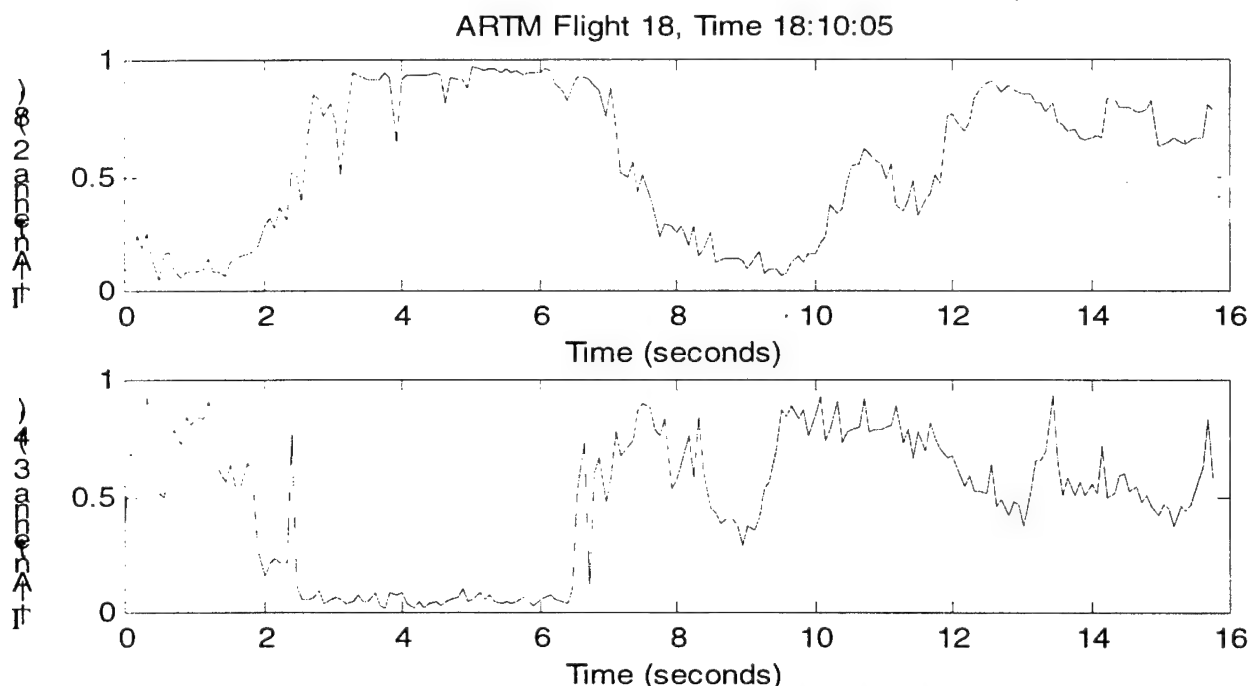


Figure 2.9: Plot of $|T|$ vs Time for Cord's Road Run (ARTM Flight 18, Time 18:10:05) at Edwards AFB with an aircraft altitude of 5,000 feet.

3 BIT ERROR PERFORMANCE ANALYSIS OF BPSK IN THE PRESENCE OF MULTIPATH FADING

Multipath reflections are *often* undesirable because they can corrupt the transmitted signal and decrease the signal performance as measured by the probability of bit error. The characteristics of the multipath signal, such as the relative amplitude (Γ), phase (γ) and delay (τ), determine the overall effect that the multipath will have on the bit error rate. When a single multipath reflection is present at the receiving antenna, the received signal can be modeled including the effects of additive noise as

$$r(t) = s(t) + \Gamma \cos(\gamma)s(t - \tau) + n(t) \quad (3.1)$$

Incorrect bit decisions can be caused by multipath interference and by noise in the channel and receiver. In general, a high signal to noise ratio will decrease the likelihood of a bit error caused by noise in the channel. However, the presence of multipath interference can degrade a high signal to noise ratio, resulting in decreased signal performance. The effects of multipath interference can be seen in a comparison of eye patterns.

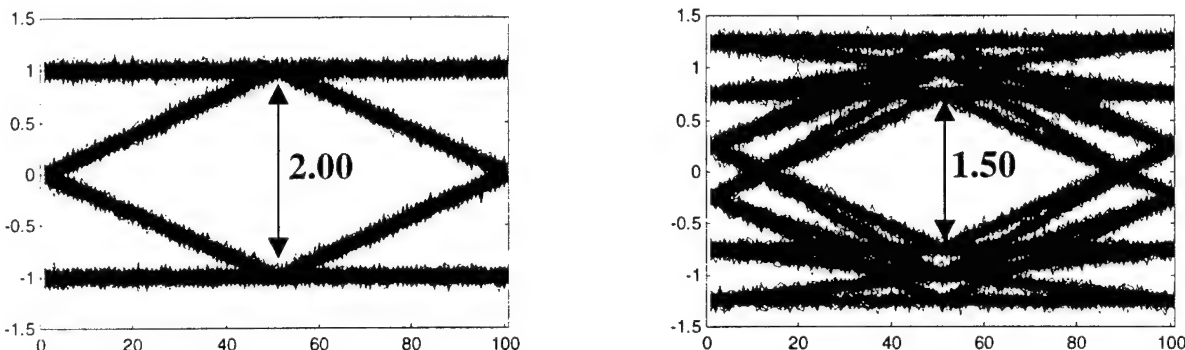


Figure 3.1: Normal Eye Pattern for BPSK signal in Gaussian noise (left) and Eye Pattern of multipath corrupted signal where $\Gamma = 0.25$ and $\tau = 2.5*T_b$ (right).

The eye diagram shows that the noise margin of the system has decreased by a factor proportional to the relative amplitude of the multipath signal [4]. Consequently the sensitivity of the receiver to timing errors has also increased. As the relative amplitude of the multipath signal increases, the “eye” will close even further, indicating an even higher probability of bit errors.

A standard BPSK demodulator makes its bit decisions based on the output of a matched filter sampled at the bit time. For a signal $s(t)$ that is corrupted by a single multipath reflection, the output of a matched filter receiver with impulse response $h(t) = \phi^*(-t)$ sampled at the bit time is given by

$$x(T_b) = \int_0^{T_b} s(t) \phi(t) dt + \int_0^{T_b} \Gamma \cos(\gamma) s(t - \tau) \phi(t) dt + \int_0^{T_b} n(t) \phi(t) dt \quad (3.2)$$

Depending on the characteristics of the multipath interference, the multipath will add either constructively or destructively to the line of sight signal. Constructive interference will increase

the signal to noise ratio and improve the quality of the bit decisions, while destructive interference will decrease the signal to noise ratio and increase the likelihood of bit errors.

Case 1: $\tau < T_b$

If the relative delay τ is constrained to be less than the bit time, T_b , then it is assured that the multipath interference will be constructive for at least a portion of the bit time as long as $-\pi/2 \leq \gamma \leq \pi/2$. Assuming equally likely symbols, the previously transmitted bit and the current bit will be identical 50% of the time. When this occurs, the multipath interference will be constructive for the entire symbol time. In this case, the matched filter response due to the multipath interference would be

$$\int_0^{T_b} \Gamma \cos(\gamma) s(t - \tau) \phi(t) dt = \pm \sqrt{E_b (\Gamma \cos(\gamma))^2} \quad (3.3)$$

When the current bit and the previous bit are opposite, the multipath component of the matched filter output is

$$\int_0^{T_b} \Gamma \cos(\gamma) s(t - \tau) \phi(t) dt = \pm \sqrt{E_b (\Gamma \cos(\gamma) (1 - 2\tau/T_b))^2} \quad (3.4)$$

If the response of the matched filter due to the noise term $n(t)$ is represented by the zero mean Gaussian random variable $W \sim N(0, \sigma^2)$, the sampled output of the matched filter is

$$x(T_b) = \begin{cases} \pm \sqrt{E_b (1 + \Gamma \cos(\gamma))^2} + W, & \text{Identical Bits} \\ \pm \sqrt{E_b (1 + \Gamma \cos(\gamma) (1 - 2\tau/T_b))^2} + W, & \text{Opposite Bits} \end{cases} \quad (3.5)$$

When the noise power is high enough to perturb the output, $x(T_b)$, beyond the decision boundary, a bit error occurs. For example, the probability of bit error when two binary “0’s” are transmitted sequentially can be expressed as

$$\begin{aligned} P(E) &= \Pr \left\{ -\sqrt{E_b (1 + \Gamma \cos(\gamma))^2} + W > 0 \right\} \\ &= \Pr \left\{ W > -\sqrt{E_b (1 + \Gamma \cos(\gamma))^2} \right\} \end{aligned} \quad (3.6)$$

The probability of bit error is obtained by integrating the upper tail of the probability density function of the noise distribution.

$$P(E|0,0) = \int_0^{\infty} \frac{1}{\sqrt{2\pi\sigma^2}} \exp \left\{ \frac{-(x-\mu)^2}{2\sigma^2} \right\} dx \quad (3.7)$$

where $\mu = -\sqrt{E_b (1 + \Gamma \cos(\gamma))^2}$ and $\sigma^2 = N_o/2$.

This integral can also be expressed in terms of the Q function

$$P(E|0,0) = P(E|1,1) = Q\left(\sqrt{\frac{2E_b \cdot (1 + \Gamma \cos(\gamma))^2}{N_o}}\right) \quad (3.8)$$

The result of Equation (3.8) also holds for the case when 2 binary “1’s” are transmitted sequentially. When the current bit and the previous bit happen to be opposite, the probability of error can be shown to be

$$P(E|0,1) = P(E|1,0) = Q\left(\sqrt{\frac{2E_b \cdot (1 + \Gamma \cos(\gamma) \cdot (1 - 2\tau/T_b))^2}{N_o}}\right) \quad (3.9)$$

Under the assumption that all bits are equally likely, application of the law of total probability yields the probability of error for BPSK when $\tau < T_b$:

$$P(E) = \frac{1}{2} Q\left(\sqrt{\frac{2E_b \cdot (1 + \Gamma \cos(\gamma))^2}{N_o}}\right) + \frac{1}{2} Q\left(\sqrt{\frac{2E_b \cdot (1 + \Gamma \cos(\gamma) \cdot (1 - 2\tau/T_b))^2}{N_o}}\right) \quad (3.10)$$

Case 2: $\tau > T_b$

If the relative delay is greater than the bit time there is the additional possibility that multipath interference will be completely destructive during an entire symbol time. When this occurs, the receiver will experience the largest possible drop in the effective signal to noise ratio. This makes the bit decisions most sensitive to noise. It can be shown that these errors will account for a majority of the total number of bit errors. The probability of error in this situation is given by

$$P(E) = Q\left(\sqrt{\frac{2E_b \cdot (1 - \Gamma \cos(\gamma))^2}{N_o}}\right) \quad (3.11)$$

When the multipath interference is completely constructive, the probability of error can be shown to be

$$P(E) = Q\left(\sqrt{\frac{2E_b \cdot (1 + \Gamma \cos(\gamma))^2}{N_o}}\right) \quad (3.12)$$

This is identical to the case above where two identical symbols are received in sequence.

When a multipath ray interferes constructively more than it interferes destructively during a single bit time, the probability of bit error is

$$P(E) = Q\left(\sqrt{\frac{2E_b \cdot (1 + \Gamma \cos(\gamma)/T_b \cdot (2((\tau))_{T_b} - T_b))^2}{N_o}}\right) \quad (3.13)$$

Similarly, when the amount of constructive interference is less than the amount of destructive interference during a single bit time, the probability of bit error is

$$P(E) = Q\left(\sqrt{\frac{2E_b \cdot (1 - \Gamma \cos(\gamma)/T_b \cdot (2((\tau))_{T_b} - T_b))^2}{N_o}}\right) \quad (3.14)$$

If we assume that the conditions represented by Equations (3.11) – (3.14) are equally likely to occur in a random binary signal, the total probability of error when $\tau > T_b$ is

$$\begin{aligned} P(E) = & \frac{1}{4}Q\left(\sqrt{\frac{2E_b \cdot (1 + \Gamma \cos(\gamma))^2}{N_o}}\right) + \frac{1}{4}Q\left(\sqrt{\frac{2E_b \cdot (1 + \Gamma \cos(\gamma)/T_b \cdot (2((\tau))_{T_b} - T_b))^2}{N_o}}\right) \\ & + \frac{1}{4}Q\left(\sqrt{\frac{2E_b \cdot (1 - \Gamma \cos(\gamma))^2}{N_o}}\right) + \frac{1}{4}Q\left(\sqrt{\frac{2E_b \cdot (1 - \Gamma \cos(\gamma)/T_b \cdot (2((\tau))_{T_b} - T_b))^2}{N_o}}\right) \end{aligned} \quad (3.15)$$

3.1 Simulation of Theoretic Results

Computer simulations were used to verify the derivation of the probability of bit error under multipath fading conditions. A NRZ BPSK signal was corrupted by simulated multipath interference with known relative amplitude, Γ , phase, γ , and delay, τ . This composite signal was subsequently demodulated using a standard matched filter receiver. The probability of error was calculated as the number of bit errors divided by the total number of transmitted bits. In all simulations a set of 100,000 random bits was transmitted and received.

In the first simulation, the characteristics of the simulated multipath interference, (Γ , τ , γ) were held constant while the signal to noise ratio was allowed to vary from 3 to 10 dB. The probability of bit error for this configuration was plotted along with that of an uncorrupted BPSK signal. As shown in Figure 3.2, when the signal is corrupted by a single multipath reflection with parameters ($\Gamma = 0.85$, $\tau / T_b = 0.80$, $\gamma = \pi/8$) the performance was decreased by approximately 3 dB. To compensate for the decreased performance of the telemetry channel due to this specific multipath interference, an additional 3 dB of link margin must be added. As the relative amplitude of the multipath signal increases, the signal performance will deteriorate even further.

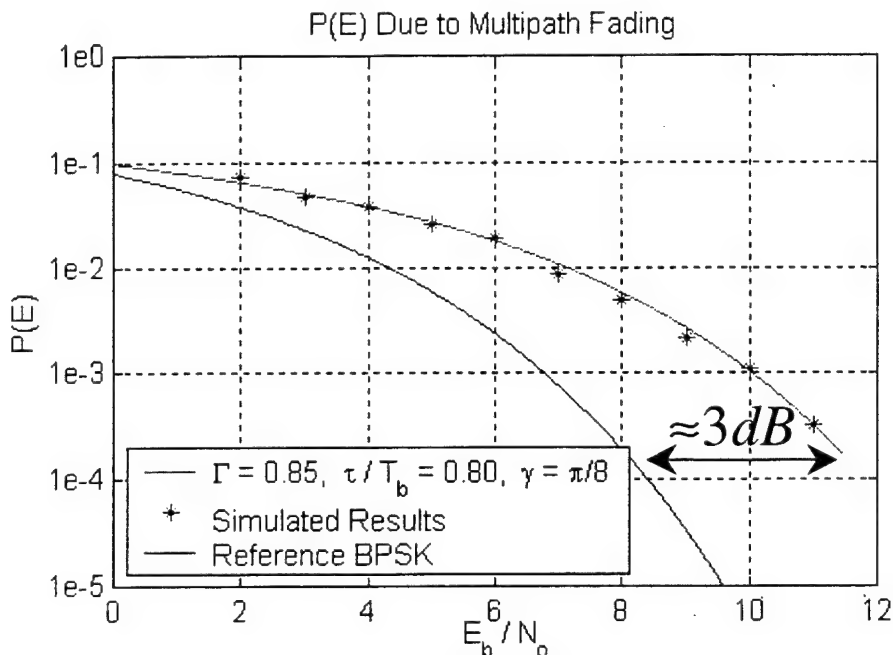


Figure 3.2: Performance comparison of BPSK and a multipath corrupted BPSK signal.

The second simulation measured the effect of the relative amplitude, Γ , and the relative phase, γ , on the signal performance as the relative delay of the multipath signal varied from 0 to 2 times the bit time. For this test, the signal to noise ratio was constant at a value of 5 dB. Figure 3.3 shows the results for two signals. The amplitude and phase of the two multipath signals are held constant at $\Gamma_1 = 0.75, \gamma_1 = \pi/8$ and $\Gamma_2 = 0.95, \gamma_2 = 0$. Because the amount of constructive interference was greater than the amount of destructive interference for $\tau / T_b < 0.5$, the overall signal performance improved dramatically due to the increased signal energy provided by the multipath reflection. However for $\tau / T_b > 0.5$ the performance rapidly decreased as the destructive interference lowered the effective SNR.

The third simulation explored the effect of a variation in the relative phase shift on the overall signal performance. As seen in Figure 3.4, when the multipath signal arrives in phase with the line of sight signal, there is an increase in the total signal power for $\tau / T_b < 0.5$ which correspondingly increases the signal performance. However, if the multipath signal arrives out of phase with the line of sight signal, there will be an attenuation of the total signal power for $\tau / T_b < 0.5$ resulting in a dramatic drop in performance.

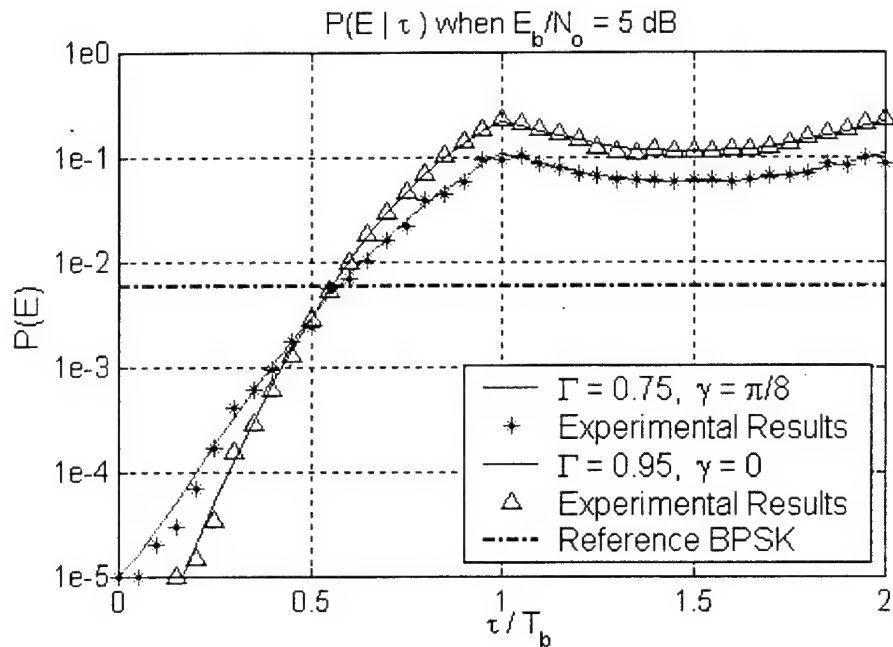


Figure 3.3: Probability of bit error as a function of the relative delay of the multipath signal.

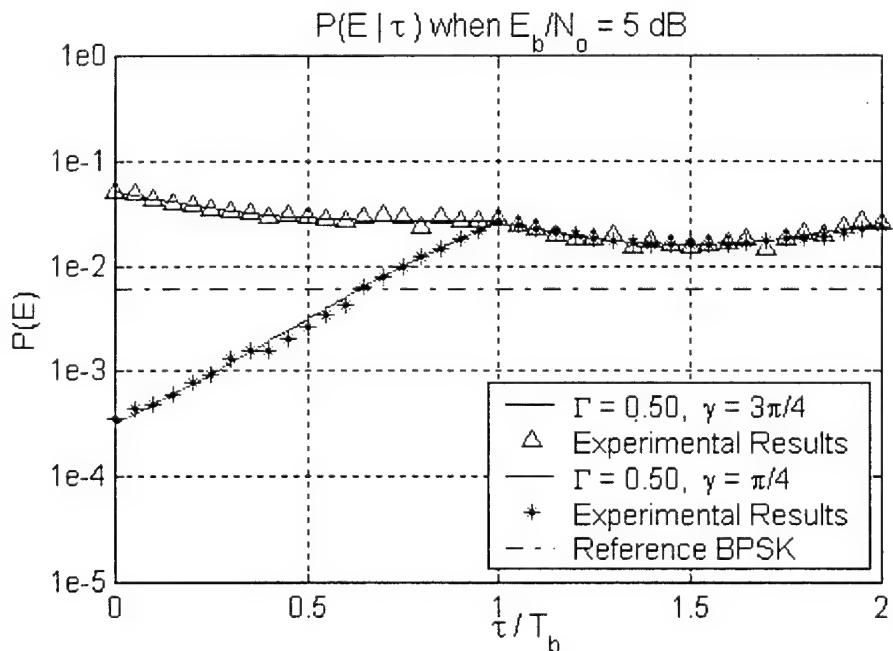


Figure 3.4: Probability of bit error as a function of the relative delay and phase of the multipath signal.

3.2 ARTM Channel Sounding Results

The ARTM test flights maintained an extremely high signal to noise ratio so that all bit errors would be independent of the additive noise and a direct result of multipath interference. Rice et al. [1] conducted channel sounding experiments at Edwards Air Force Base and estimated the characteristic parameters of the multipath fading that occurred. The actual probability of bit error was correlated with the multipath characteristics at specific times. The results indicate that while large amplitude reflections cause the most severe increases in bit error rates, even relatively small multipath reflections can cause significant increases in the bit error rate. This conclusion is supported by the dependence of the bit error rate on the relative phase and delay of the multipath reflection.

Two characteristic examples of the ARTM channel sounding data are shown below. These examples illustrate the effect of multipath fading on the spectrum of the received signal. Figure 3.5 displays the results of a “long-delay” multipath reflection with a relatively small amplitude. Figure 3.6 is typical of a “short-delay” multipath signal with significant relative amplitude.

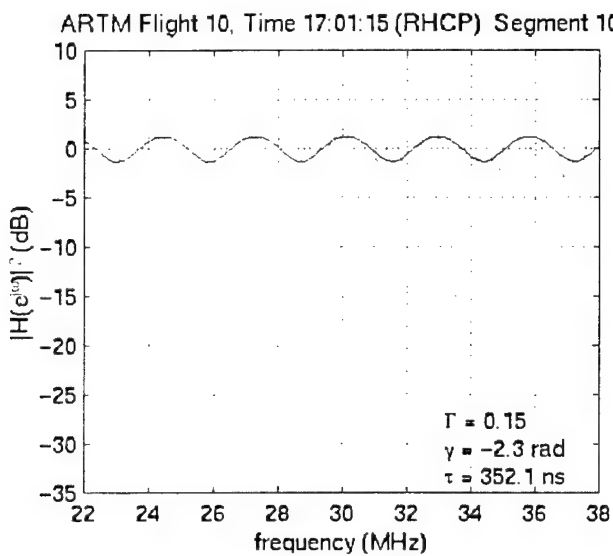


Figure 3.5: “Long-delay” multipath fading.

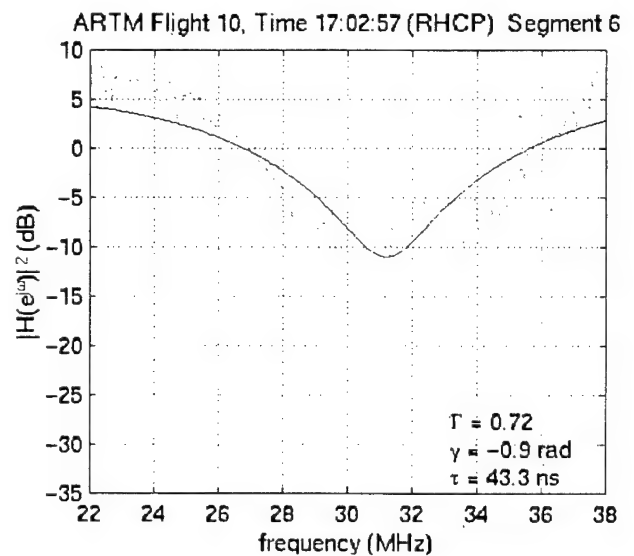


Figure 3.6: “Short-delay” multipath fading

Based on the estimated multipath characteristics of the channel sounding data in Figures 3.5 and 3.6, Equations (3.10) and (3.15) were used to estimate of the probability of bit error for these two channels. The signal to noise ratio, E_b/N_o , was estimated based on the range of the aircraft during the fade events. The calculation of the theoretical bit rate does not account for the effects of symbol timing offset and carrier phase recovery. For these reasons the calculated bit error rate will be an approximation to the actual bit error rate that one could expect in a real communications system. Table 3.1 shows the agreement between the estimated bit error rate and the observed bit error rate.

Table 3.1: Comparison of measured bit error rate and calculated bit error rate for multipath fading characterized by Figures 3.5 and 3.6.

	Γ	γ	τ	Measured Bit Error Rate	Estimated Bit Error Rate
Figure 6	0.15	-2.3 rad	352.1 ns	5.50×10^{-6}	6.31×10^{-6}
Figure 7	0.72	-0.9 rad	43.3 ns	5.00×10^{-3}	5.70×10^{-3}

4 DYNAMIC BEHAVIOR OF MULTIPATH INTERFERENCE IN ARTM CHANNEL SOUNDING DATA

Several features of the ARTM channel greatly influence the amount of the multipath interference present and the amount of dynamics seen in this interference. First of all, the transmitter is on a T-39 Saberliner jet flying at altitudes of 5000 and 10,000 ft. During the channel sounding runs the plane flies over terrain that reaches altitudes of 6000 ft. Because of these low altitudes there are many reflectors close to the LOS path. The signal is being received by parabolic antennas. Since these are very directional antennas, a reflected signal cannot deviate far from the LOS path and still arrive in the main lobe of the antenna. Thus, low altitudes mean more objects will be close to the LOS path, which in turn will greatly increase the likelihood of strong multipath reflections.

Another important characteristic of the ARTM channel is that the signal is wideband. This allows for the frequency selective nature of the multipath interference to be seen. It will also show how the multipath fades evolve over time in the frequency domain.

It has been shown that the ARTM channels can be adequately modeled by a LOS transmission with one or two multipath reflections [2]. For simplicity, we will limit our discussion to a two-ray model, which includes the LOS signal and one multipath reflection. The impulse function for a two-ray model would therefore consist of a LOS transmission and a scaled, time delayed, and frequency and phase shifted version of itself, or

$$h(t) = \delta(t) + \Gamma e^{j(2\pi f_0 \tau + \theta)} \delta(t - \tau) \quad (4.1)$$

where Γ is the magnitude of the reflection, θ is the phase shift caused by the reflective medium, τ is the delay of the reflection, and $2\pi f_0 \tau$ is the phase shift caused by the delay (f_0 is the carrier frequency). We are concerned only with the overall phase shift, so we simplify the expression by representing the total phase shift as $\gamma = 2\pi f_0 \tau + \theta$. The magnitude of the corresponding channel transfer function is

$$|H(f)|^2 = 1 + \Gamma^2 + 2\Gamma \cos(2\pi f \tau - \gamma). \quad (4.2)$$

Thus we see that a multipath fade event causes frequency selective interference.

4.1 Dynamics of the Channel Model

We can now analyze this model with respect to our parameters to gain insight into how the multipath fade event evolves over time. The simplest example of multipath interference would be a single reflection from an object on the ground between the plane and the receiver. As the plane flies along, its position changes very rapidly. This will cause the distance the reflected signal travels to change, which will in turn change the delay, τ , and phase, γ , of the multipath component of the signal at the receiver. The magnitude of the reflection, Γ , may also change since the point of reflection for the multipath signal would likewise change position and may be reflecting from a different object. Γ may also decrease due to the fact that the change in position may change the angle of incidence such that the reflection is no longer arriving in the main lobe of the receiving antenna.

Using our channel model we will now show how a change in the position of the aircraft will affect our multipath interference. Figure 4.2 shows a typical multipath fade from our channel sounding data. Our model parameters have been selected to approximate this fade. The parameter values are shown on the graph. The smooth line indicates the modeled fade.

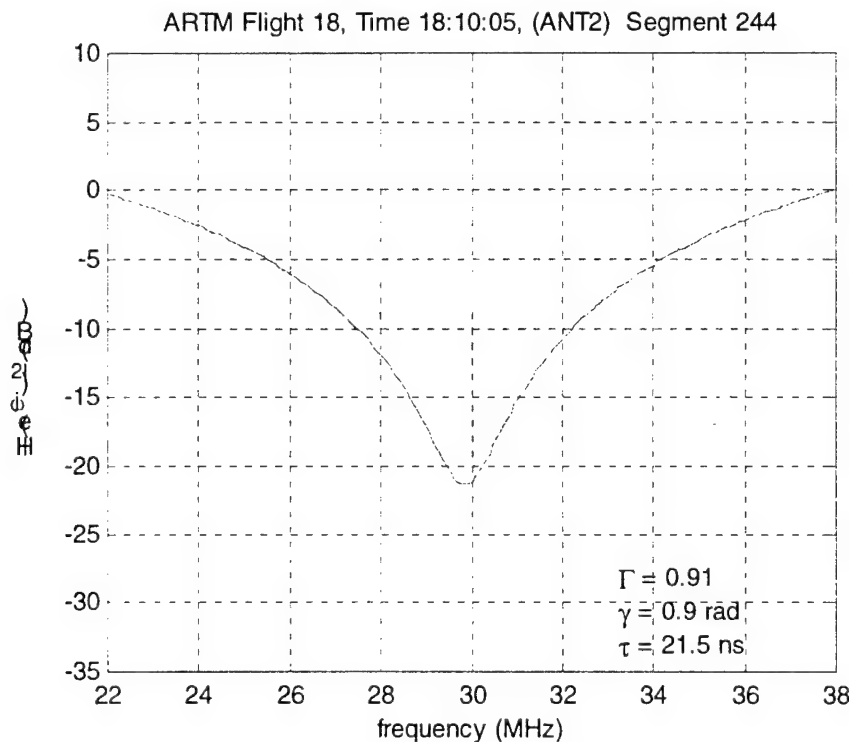


Figure 4.2: Magnitude squared transfer function, $|H(f)|^2$, for the channel sounding data showing a multipath fade event. The smooth line indicates the channel model approximation to this fade.

From Equation (4.2) we are able to see how slight change in the environment will effect the multipath fade event. First we note that the depth of the fade is determined by the strength of the

reflection, Γ . As the position of the aircraft moves, the differential path length between the LOS signal and the reflected signal also changes. This will change the relative phase and delay of the reflected signal, which will change the frequency and phase of the cosine term of Equation (4.2). Thus, slight changes in position will change the frequencies affected by the multipath fade. We expect to see all combinations of these types of changes in our data.

As we compare changes in the environment with changes in a multipath fade event, it is important to realize that it is not the speed of the aircraft that we are concerned with, but the rate at which the differential path length between the LOS signal and the multipath reflection is changing. If the airplane is flying along at hundreds of feet per second, the differential path length may be changing only a few feet per second or less depending upon the height of the aircraft and the distance from the receiver. It is also important to note that it is only the radial component of the velocity vector of the plane (see Figure 4.3) that will effect the differential path length.

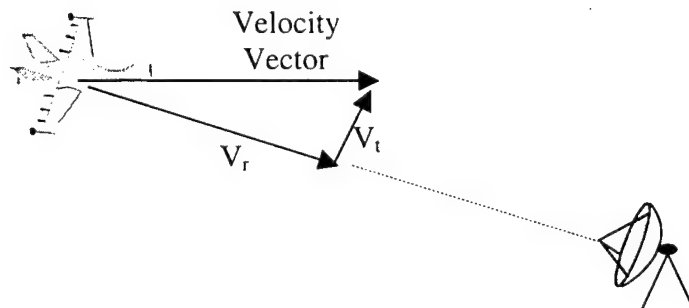


Figure 4.3: Shown are radial, V_r , and tangential, V_t , components of the velocity vector, V , of the aircraft. Only changes in the radial component will change the differential path length and effect the phase and delay of the multipath reflection.

For example, Figure 4.4 shows the terrain for Flight 18 above the Black Mountains north of Edwards EAFB. The speed of the aircraft is 200 knots (89 m/s). If we assume that the reflection is somewhere along the halfway point between the plane and the receiver and that there is no tangential component of the velocity vector, then the differential path is changing at a rate of 36 cm/s. The differential path is changing 250 times slower than the aircraft is moving. The carrier for the signal is at 1460 MHz, with a wavelength of 20 cm. If the differential path changes at a rate of almost 40 cm/s, the phase of the fade could move 180 degrees in about a quarter of a second. Therefore, points of constructive interference could change to points of destructive interference in a quarter of a second. This gives us a good ballpark estimate for the rate of change for the phase of the multipath fades.

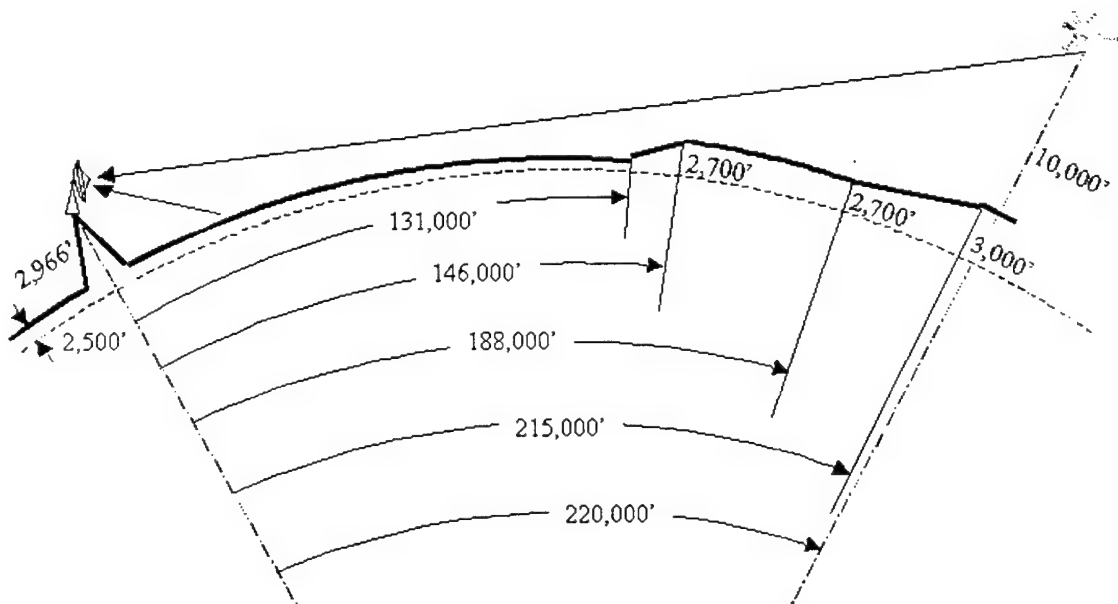


Figure 4.4: Terrain of the black mountain run for flight 18.

Using our channel model, we can simulate a changing fade event at this location. In 800 ms the differential path length will change 28.8 cm. This will move the phase of the reflected signal 9.0 rad, and the delay will change 0.94 ns. The resulting multipath fade is plotted in Figure 4.5. Since the phase of the fade changed more than 2π , the fade cycled back around through our range of frequencies. From this we realize that small changes in the position barely alters the delay but drastically changes the phase of the multipath reflection. Thus, a fade is much more sensitive to changes in phase of the reflection.

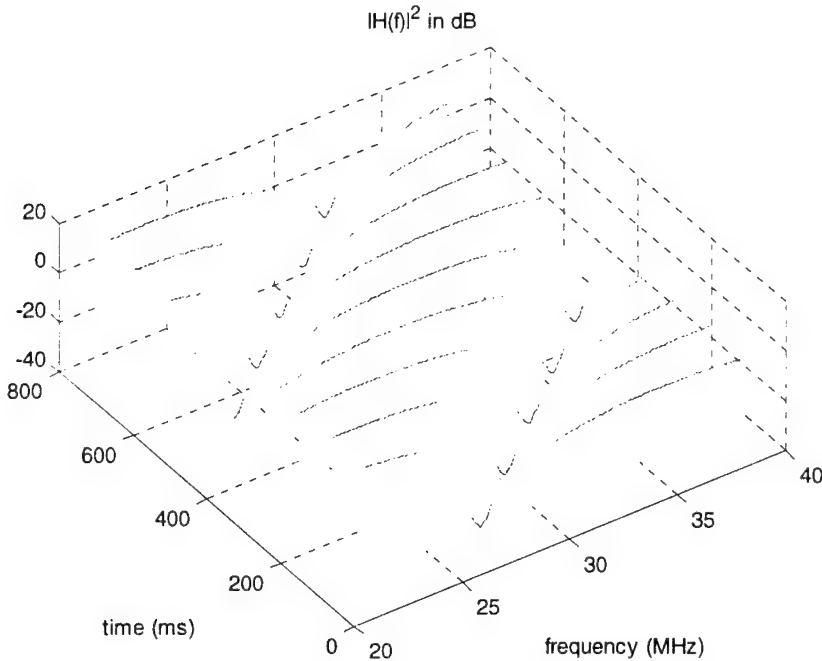
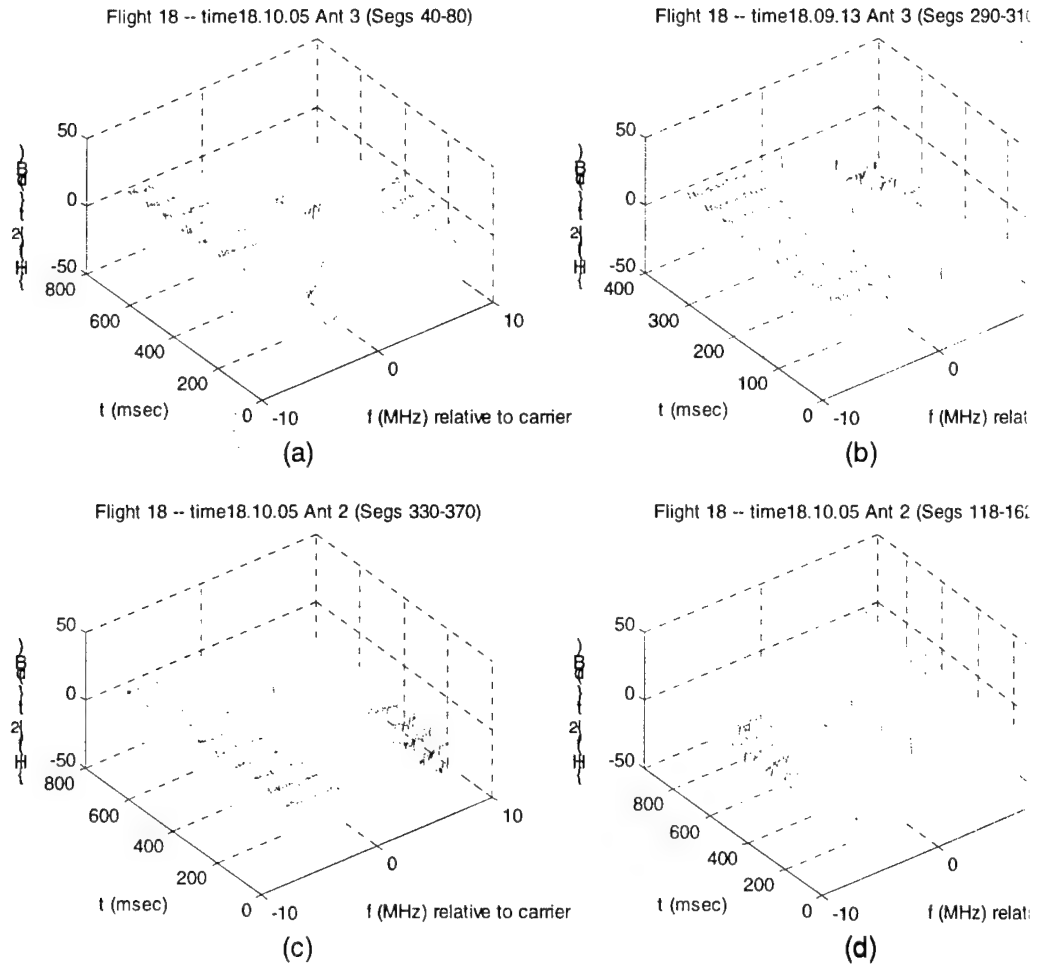


Figure 4.5: Simulated multipath fade event, showing the frequency changes due to the changing differential path length between the LOS signal and the reflected signal caused by a change in the position of the aircraft.

4.2 Dynamics of the Channel Sounding Data

We are now ready to look at some of the data to see how the multipath fades are changing over time in the channel. Shown in Figure 4.6 are four examples of multipath fade events. The channel has been sampled every 20 ms and each part of Figure 6 shows selected slices of the magnitude squared transfer function, $|H(f)|^2$. In order to make the graphs more readable, only every forth or every second segment has been included. In Figure 4.6a we see that a fade event is present at the beginning of the sampled data in the lower frequency range. It meanders across the frequency range until it dies out almost a full second later. One explanation for this would be a change in phase due to the differential path length changing. The fade sweeps half of the frequencies in about 0.5 seconds, which is consistent with the rate of change previously hypothesized with our channel model. In Figure 4.6b the fade slowly grows to a large value over several samples of the channel, but it is difficult to say whether or not this is because the fade diminished in strength or simply moved out of the visible range of frequencies. The same thing happens in Figure 4.6c; except here, we see the end of the fade instead of the beginning. Figure 4.6d seems to capture both sides of the fade enough to say that the fade dies out by diminishing in magnitude instead of moving out of our range of visible frequencies. This could be due to the fact that the reflecting signal is diminishing in magnitude or the reflecting angle is moving out of the main lobe of the receiving antenna. Regardless of how, we conclude that this shows a change in the magnitude of Γ .



4.2.1.1.1

Figure 4.6: Each plot shows selected segments of the magnitude squared channel transfer function, $|H(f)|^2$, from ARTM Flight 18. Only every forth or every second segment has been included in the plots

4.3 Doppler Bandwidth Characterization of Channel Dynamics

We now quantify the exact rate at which our channel is changing. Our goal here will be to determine how the multipath fade events can be viewed as time-invariant. The Doppler power spectrum is a powerful way of doing this [5].

The most important characteristic of the Doppler power spectrum is the Doppler bandwidth, B_d . The Doppler bandwidth, or Doppler spread, is defined as the range of values for which the Doppler power spectrum is essentially nonzero [6]. Along with the absolute Doppler bandwidth, it is also instructive to look at the 95%, 97%, and 99% power bandwidth. However defined, the Doppler bandwidth is a measure of the rate at which our channel is changing and has units of Hertz. Taking the inverse of the Doppler bandwidth gives us the coherence time, (Δt_C):

$$(\Delta t_c) = \frac{1}{B_d} . \quad (4.3)$$

The coherence time, with units of seconds, tells us how long the channel may be viewed as a time-invariant system.

Shown in Figure 4.7 are the corresponding Doppler power spectrums for each of the channel transfer functions plotted in Figure 4.6. Notice that Figure 6a contains a fade that sweeps across the entire frequency band. It contains noticeably more change than the other three plots. The corresponding Doppler power spectrum, shown in Figure 4.7a, contains the most overall power of the four spectrums.

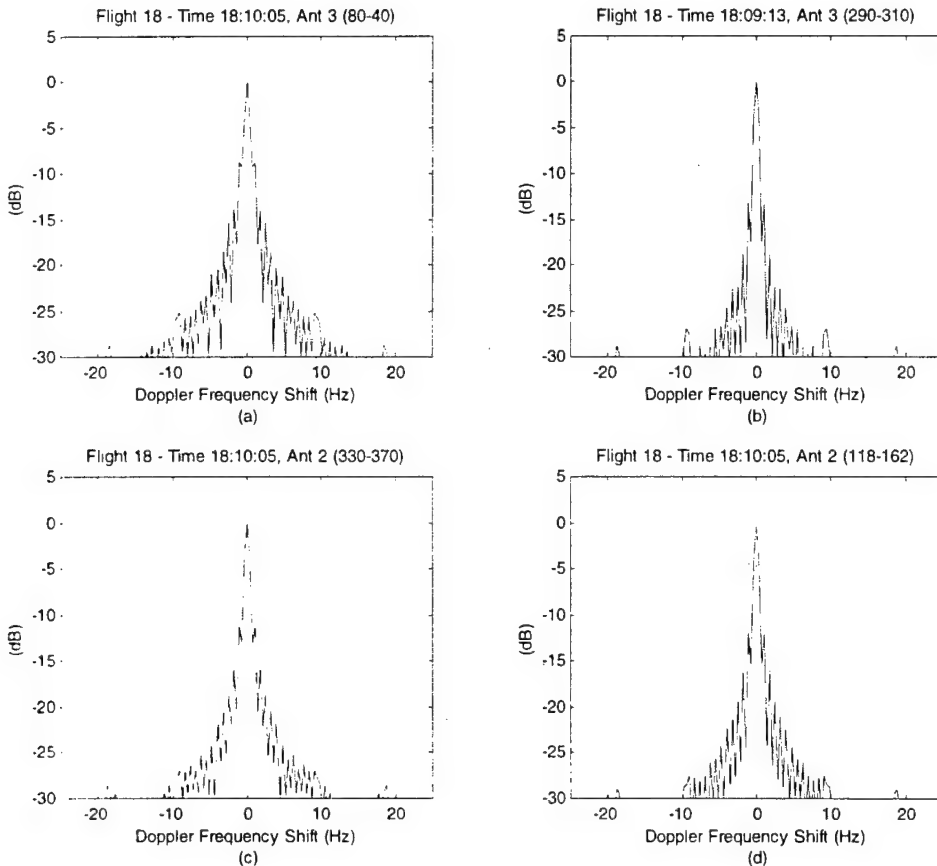


Figure 4.7: Doppler Power Spectrum for each multipath fade shown in Figure 5.

Calculated in Table 4.1 are the 95%, 97%, 99% power bandwidths, and the absolute bandwidth for each Doppler power spectrum in Figure 4.7. Since there are small side lobes at high frequencies, the absolute bandwidth would appear to be a poor measure of the Doppler bandwidth. However, this would depend upon how sensitive a particular application is to the changing fades. The absolute bandwidth would give a measure of the highest frequency of change present in the multipath interference even if there is low energy at these frequencies. A

more appropriate measure of the Doppler bandwidth might be the 99% power bandwidth. The 99% power bandwidth is almost half the size of the absolute bandwidth for each spectrum and includes almost all the power in the spectrum. Also note that Figure 4.7a, which represents the rapidly changing channel, has the highest bandwidths in all cases. But the absolute bandwidth does not indicate much difference in the four spectrums. However, in the 97% bandwidth Figure 4.7a has nearly twice the bandwidth than the other three spectrums. Thus, the power bandwidths give a much better indication of how much change is present in the data.

Figure	95% Power Bandwidth (Hz)	97% Power Bandwidth (Hz)	99% Power Bandwidth (Hz)	Absolute Bandwidth (Hz)
7a	3.2609	5.4348	9.7826	19.0542
7b	1.0870	2.5362	6.1594	18.9911
7c	2.5362	4.3478	9.0580	19.0402
7	1.8116	3.2609	7.6087	18.9742

Table 4.1: 95%, 97%, and 99% power bandwidths and absolute bandwidth for the Doppler power spectrums in Figure 4.7.

An appropriate Doppler bandwidth for these fades would be 10 Hz. This would encompass all the power in the four spectrums examined in this paper. The coherence time would therefore be 100 ms. The fade events can therefore be viewed unchanging for 100 ms. Any type of adaptive equalization would have to be able to update itself within 100 ms to effectively mitigate this interference. Of course, these values are dependent upon how one defines an acceptable noise floor.

5 PARAMETRIC ESTIMATION OF THE SCATTERING FUNCTION FOR ARTM CHANNEL SOUNDING DATA

The scattering function offers an easy way to visualize the time-dependent behavior of a channel and provides easy access to descriptive parameters such as the Doppler bandwidth and coherence time of the channel. This affords a quick way to visualize large amounts of data and notice certain trends. The most intuitive way to arrive at the scattering function is to take the Fourier transform of channel sounding data taken at successive intervals. But this is not the only way to arrive at the scattering function and it has certain limitations. A data based computation of the scattering function requires large amounts of data storage and can be very cumbersome. Certain issues are quickly lost in the detail, such as the relationship between the channel behavior and the geometry of the channel.

By computing the scattering function from a three-ray parameterization of the channel sounding data, one can achieve a great deal of insight and data compression over the data based computation. Such a parameterization provides a direct link between the channel behavior, including the time-motion of frequency nulls, and the geometry of the channel. Such a parameter based approach also reduces the data of each snapshot of the channel to just two information triplets. Because of the data compression, some features of the scattering function are naturally lost, but the loss of information is surprisingly small. This paper examines a

parameter based approach of quantifying the channel dynamics and applies this technique to the ARTM channel sounding data.

5.1 Mathematical Development and Modeling Assumptions

We now consider the methods used to generate our parameter based estimates of the scattering function. By definition, the scattering function corresponds to a Fourier transform of the autocorrelation of a two-dimensional channel impulse function [6,8]. An appropriate model of the ARTM channel impulse response function, $h(\tau, t)$, is the normalized three-ray model [1,5]

$$h(\tau, t) = \delta(\tau) + \Gamma_1(t)\delta(\tau - \tau_1(t)) + \Gamma_2(t)\delta(\tau - \tau_2(t)). \quad (5.1)$$

Here, τ represents the time delay between the arrival of various components of the signal, such as the line-of-sight component and the first and second reflections of the signal. The variable, t , represents time, making clear that the behavior of our channel changes over time. This is certainly to be expected over the duration of a flight traversing uneven terrain. The function, $\delta(t)$, is the unit impulse function, which is equal to one at $t = 0$ and is zero elsewhere. The function $\Gamma_i(t)$ is the complex gain of the i^{th} component of the signal relative to the LOS path.

To derive the scattering function from this equation, we must first take a two dimensional correlation of the channel impulse response function of Equation (5.1) in both t and τ [6,8]. For our channel, the direct computation is unnecessarily complex. Instead, we are justified in making a number of simplifying assumptions, due to the physics of our channel [5]. Accordingly, we may state the following:

Assumption 1: the phase can be treated as being independent from both the delay and the magnitude.

Assumption 2: the phase is distributed uniformly over $(-\pi, \pi]$.

Assumption 3: $\Gamma_1(t)$ and $\Gamma_2(t)$ are uncorrelated, an assumption known as *uncorrelated scattering* in communications literature [5,6,8].

Assumption 4: the channel is wide sense stationary (WSS).

Taken together, these assumptions allow us to arrive at the following relationship to express $R_{hh}(\tau, \Delta t)$, the time-delay correlation of the channel impulse response function [5]:

$$\begin{aligned} R_{hh}(\tau, \Delta t) &= \delta(\tau)\delta(\tau) + E\{\Gamma_1^*(t)\delta(\tau - \tau_1(t))\Gamma_1(t + \Delta t)\}\delta(\tau - \tau_1(t + \Delta t)) \\ &\quad + E\{\Gamma_2^*(t)\delta(\tau - \tau_2(t))\Gamma_2(t + \Delta t)\}\delta(\tau - \tau_2(t + \Delta t)) \end{aligned} \quad (5.2)$$

Here, the operator $E\{x\}$ means the expected value of x , and the asterisk means the complex conjugate of the function. In its present form, Equation (5.2) corresponds to the bubble denoted “Formula with mathematical expectations” in Figure 5.2. Because we are interested in generating $R_{hh}(\tau, \Delta t)$ and the scattering function from a finite set of data, we estimate the function

by a conditional form of a sample correlation. Naturally we can only estimate the scattering function for the discrete samples taken at times $t = kT_s$, where T_s is the sampling interval. $R_{hh}(\tau, kT_s)$ may be approximated at these points as [5]:

$$\begin{aligned} R_{hh}(\tau, kT_s) \approx & \delta(\tau)\delta(\tau) + \frac{N(\tau,1)}{N} \frac{1}{|J_1(\tau, kT_s)|} \sum_{j \in J_1(\tau, kT_s)} \Gamma_1^*(jT_s) \Gamma_1((j+k)T_s) \\ & + \frac{N(\tau,2)}{N} \frac{1}{|J_2(\tau, kT_s)|} \sum_{j \in J_2(\tau, kT_s)} \Gamma_2^*(jT_s) \Gamma_2((j+k)T_s). \end{aligned} \quad (5.3)$$

In this equation, $N(\tau, n)$ is the number of points in the partition of the parameterized data such that $\tau_n(t) \in [\tau - \Delta\tau, \tau + \Delta\tau]$, and N is the total number of data points. The set J_n is defined as follows [5]:

$$J_n(\tau, k) = \{j \mid \tau - \Delta\tau \leq \tau_n(jT_s) < \tau + \Delta\tau \text{ and } \tau - \Delta\tau \leq \tau_n((j+k)T_s) < \tau + \Delta\tau\}. \quad (5.4)$$

One may select a value $\Delta\tau$ to trade off between higher resolution of the scattering function and greater accuracy in representing the way that $\delta(\tau - \tau_n(t))$ is highly τ -selective and zeros out terms when $\tau \neq \tau_n(t)$. Equations (5.3) and (5.4) are enough to estimate the correlation function, $R_{hh}(\tau, kT_s)$, from parameterized data. The relationship of this function to the scattering function is given in Equation (5.5).

$$S_c(\tau, \nu) = \mathcal{F}_{kT_s} \{R_{hh}(\tau, kT_s)\}. \quad (5.5)$$

As indicated above, the relationship between the correlation function $R_{hh}(\tau, kT_s)$ and the scattering function, $S_c(\tau, \nu_n)$, is a Fourier transform with respect to the sampled time variable, kT_s . We use the DFT to compute this transform for finite collections of parameterized data. In Equation (5.6), the Doppler power spectrum, $S_c(\nu_n)$, is derived from the scattering function as follows [6]. We compute this integral as a sum over our finite data sets.

$$S_c(\tau, \nu_n) = \int_{-\infty}^{\infty} S_c(\tau, \nu) d\nu. \quad (5.6)$$

5.2 Estimating the Scattering Function

The most direct way to estimate the scattering function is to move directly from a magnitude squared representation of channel sounding data to sample correlation functions via the Fourier transform [5,7] as shown in Figure 5.1.

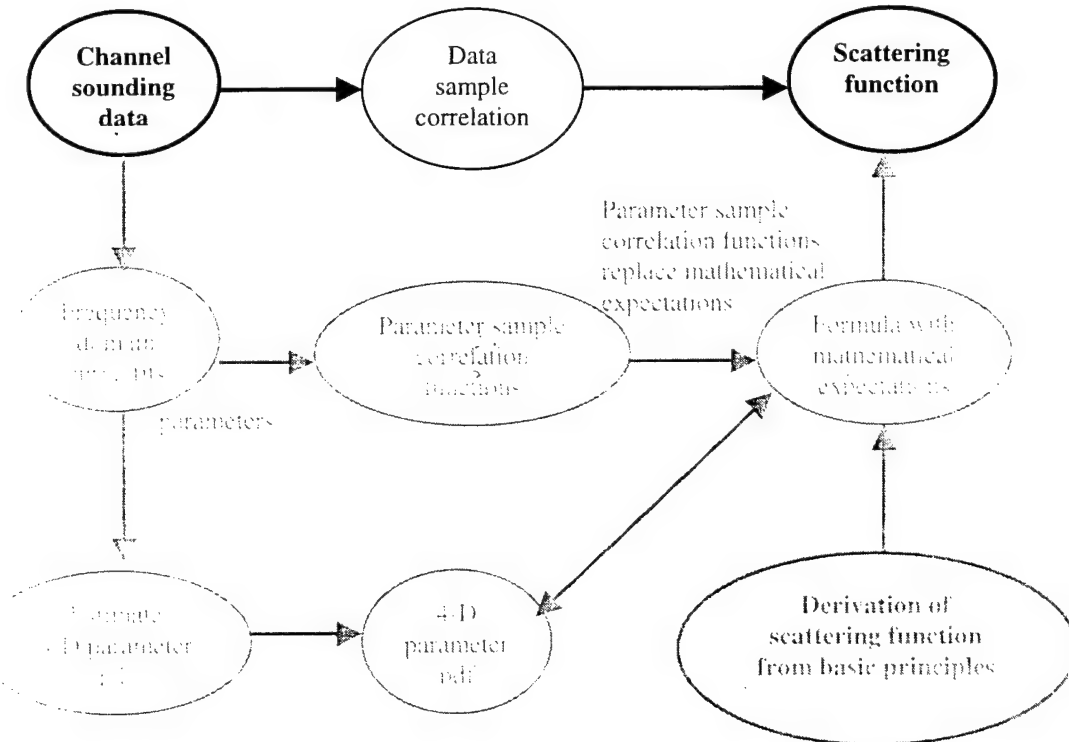


Figure 5.1: Direct Estimation of the Doppler Power Spectrum

In this section, we explore a second method of estimating the scattering function from a parameterization of the data as shown in Figure 5.2. Due to certain benefits offered by first parameterizing the data, we work with parameter-based correlation functions rather than directly with the data. Parameterized data offers at least two advantages that full data sets cannot. First, parameterized data can take considerably less storage space than full data sets. In the examples of parameterized ARTM channel sounding data considered in this paper, 12,700 data points are well described by 20 ordered triples [15]. Second, parameterized data may directly offer physical information about the channel that is hard to read from the data. It has been shown that a three-ray model representing a line-of-sight path and two reflections from physical features of the terrain near the receiver and transmitter, agrees very well with ARTM channel sounding data. Thus, such a parameterization links the data with a physical understanding of the terrain. This may help design simulations and tests that do not require costly flights.

As an example of the advantages of working with parameterized data, consider the parameter values given in Table 1 as estimated by least square fits described in [1] for the ARTM Flight 10. As described in [1], the Γ_i 's represent a (unitless) attenuation relative to the LOS path, the γ_i 's represent the phase shift in radians relative to the LOS path, and the τ_i 's represent the delay in nanoseconds between the arrival of signal power along the LOS path and the arrival of signal power along the i^{th} path. These 20 parameter triplets summarize some 12,700 data points of measured data and represent a compression factor of more than 210—a considerable reduction in the need for data storage.

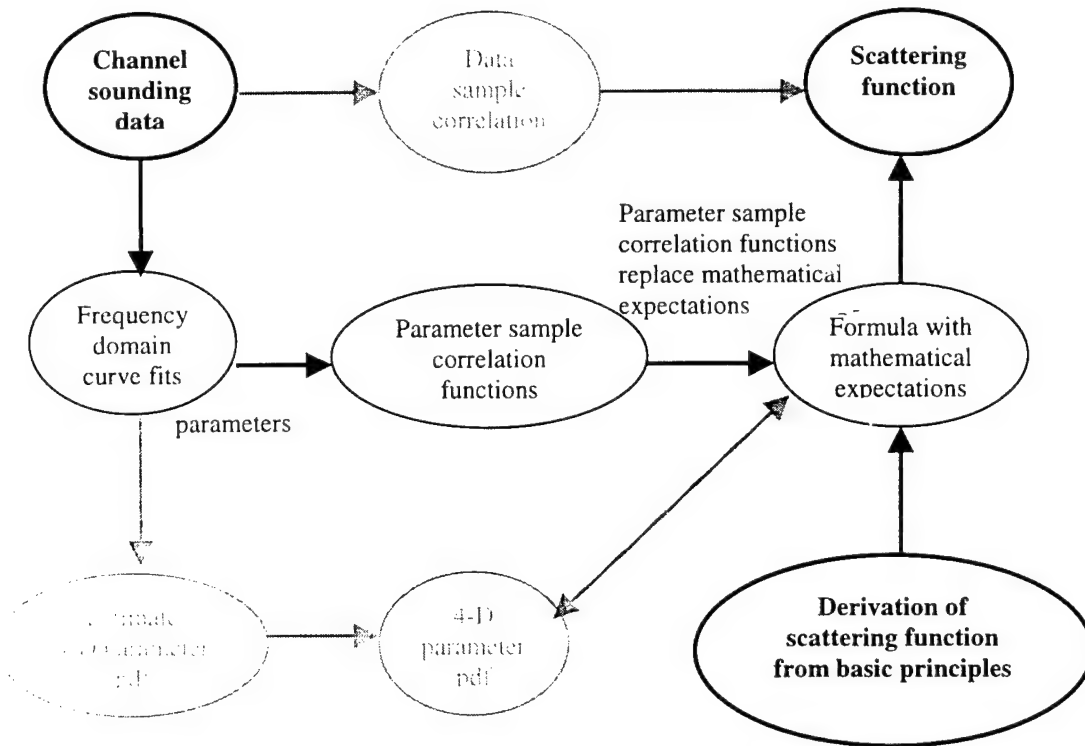


Figure 5.1: Estimation of the Doppler power spectrum from a parameterization of the data.

These parameterized data also offer a more intuitive understanding of the physical system than the raw data does. Where the ARTM channel sounding data for this flight consist of a long list of voltage levels, these parameters summarize elements of the topology of the terrain traversed during Flight 10. The first three columns of data in Table 5.1 tell us something about the first non-LOS component of the signal and the last three columns tell us about the second non-LOS component. A first glance suggests that the first non-LOS component is strongest relative to the LOS component at index points 1, 2 and 9, while the second component is strongest at index points 9 and 10. This indicates that for these samples of the channel behavior, the angles and positions of reflective surfaces are aligned with the transmitter and receiver. It also indicates that the potential for constructive and destructive interference is greatest at these times. Because the data set is small and closely related to the physics of our channel, we gain insight into the channel directly from the parameters. In fact, one might consider simulating other channels by altering our parameter set.

Despite considerable compression, the data of Table 5.1 is sufficient to generate the plots of the scattering function and Doppler power spectrum [7] in Figure 5.3, through techniques outlined in the next section. Both plots agree surprisingly well with the plots of Figure 5.4, which were computed directly from the data as diagrammed in Figure 5.1 or as outlined in [7]. In this and subsequent figures, power levels are plotted with respect to two variables, τ and v_n . The variable τ represents the time delay between the arrival of various components of the signal and the variable v_n represents the normalized Doppler shift. The Doppler shift indicates the apparent change in frequency of the signal arriving at the receiver relative to the frequency it would have,

had it arrived by the LOS path [5]. The normalized form given in this paper is computed by dividing out the dependence of the Doppler shift on the velocity of the source and the angle between the direction of travel and the line connecting the source and receiver [5].

index	Γ_1	γ_1	τ_1	Γ_2	γ_2	τ_2
1	0.93	0.3	46.2	0.04	-2.4	182.6
2	0.90	-1.9	35.4	0.06	2.7	176.3
3	0.82	0.3	48.5	0.07	-1.2	113.0
4	0.86	-2.0	36.6	0.06	-1.6	107.8
5	0.83	-2.7	33.9	0.08	0.6	148.5
6	0.77	2.0	58.4	0.09	-0.6	205.2
7	0.83	-2.0	70.4	0.14	-2.0	344.6
8	0.75	-1.6	72.9	0.14	-3.1	339.9
9	0.93	2.0	59.3	0.30	1.4	306.5
10	0.84	0.1	83.8	0.35	-0.6	296.2

Table 5.1: Parameter values estimated by least square fits as described in [1] for the ARTM Flight 10 channel at time 17:30:11 [5].

Consider first the scattering functions of Figures 5.3 and 5.4. The two are visually quite similar. Each has a large peak at the center, and as one moves out from $v = 0$, the level drops but then levels off. Moving out from $\tau = 0$, the level drops even more rapidly. It is reasonable that this basic shape should be common to both plots, as the LOS component dominates the signal. The dominance is reflected in the central peak which is at the point of no delay and no Doppler shift from the LOS path. The power level is naturally lower for signals arriving with increasingly non-zero delays and Doppler shifts. Looking a little closer at the two plots, we notice that most of the power arrives at a delay, τ , of less than 100 ns. But there is also a noticeable ridge of power around 250-300 ns in each plot indicating that there is a non-LOS path with that delay. The resolution is simply not fine enough to resolve what the delay of the first non-LOS path has.

The agreement is also rather striking in the Doppler power spectra of Figures 5.3 and 5.4 despite some variations. Each consists of a central peak that drops steadily to -30 dB by about $v_n = 0.03 \text{ m}^{-1}$ and each has significant power levels at Doppler shifts near $v_n = 0.06 \text{ m}^{-1}$. There are also noticeable differences between the two plots. The first important difference is that the data based plot of Figure 4b drops off again near $v_n = 0.08 \text{ m}^{-1}$. Second, the jumps in the level as v_n increases are more rounded and gradual in the parameter-based plot of Figure 5.3. Further, the plot of Figure 5.3 has a somewhat narrower region around $v_n = 0$ over which the signal level is between -10 and -15 dB. In general these differences can be attributed to a loss of information due to parameterizing the data [5]. Our 20 triplets of data constitute a sparse representation of the original 12,700 points and this leads to a certain rounding of features and an inability to capture some of the smaller trends in the data.

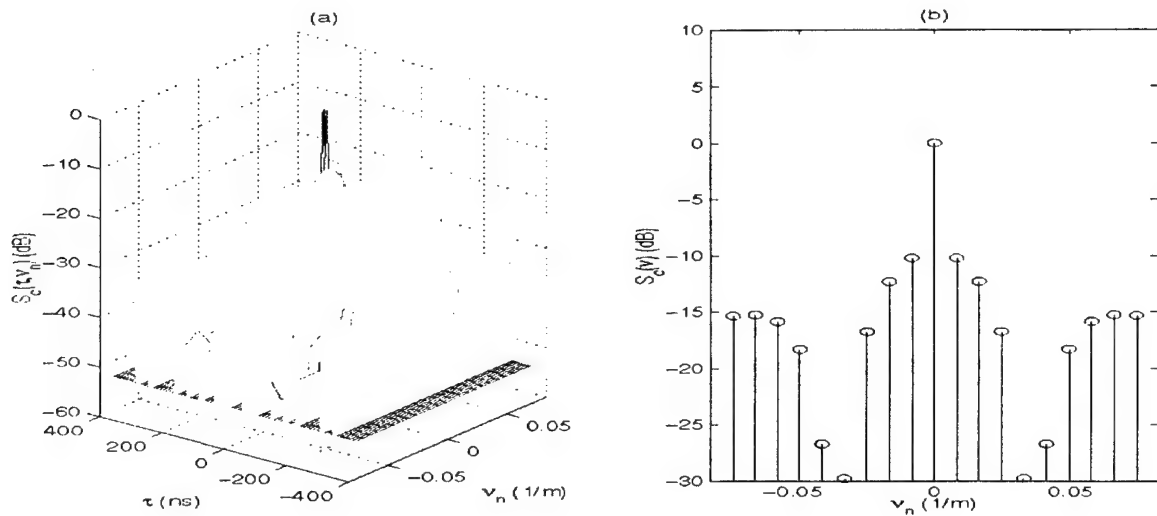


Figure 5.2: Parameter based estimates of (a) the scattering function, $S_c(\tau, v_n)$ and (b) the Doppler power spectrum, $S_c(v_n)$ of ARTM Flight 10 at 17:30:11 as diagrammed in Figure 5.2.

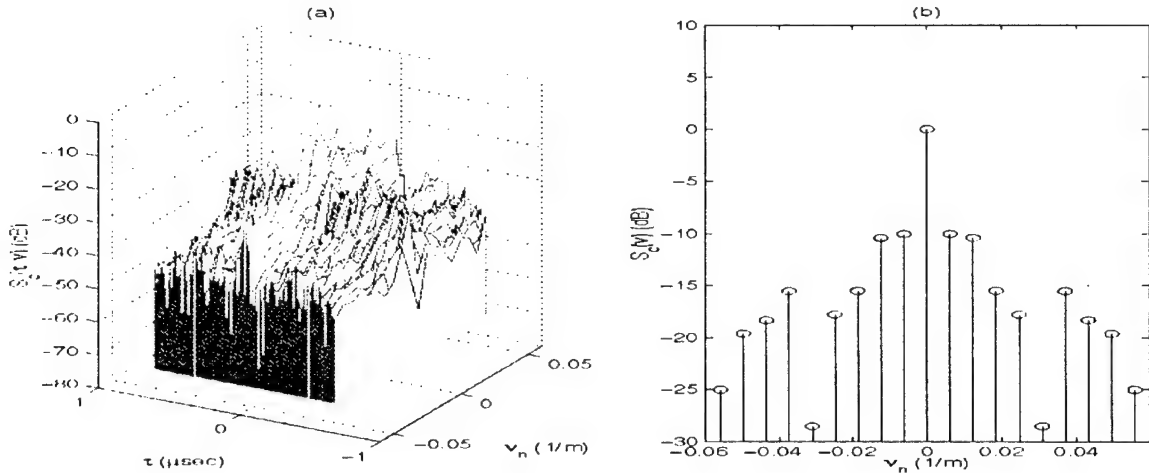


Figure 5.3: Data based estimates of (a) the scattering function, $S_c(\tau, v_n)$ and (b) the Doppler power spectrum, $S_c(v_n)$ of ARTM Flight 10 at 17:30:11 as diagrammed in Figure 5.1.

Still, the agreement is impressive. We can read from each that there is around -10 dB of power arriving with a Doppler shift very near zero and this level drops off quickly. We can also see that the Doppler bandwidth exceeds our window of observation (6.7 Hz [7]) in each case, so the coherence time must also be shorter than our snapshot spacing in time. At least in this example, either estimate tells us roughly the same details about the time-variant behavior of our channel.

5.3 A Comparison of Scattering Function Estimates for Varied Channel Behaviors

To better understand how well the parameter based technique of Figure 5.2 compares with the data based approach of Figure 5.1, we consider two further examples. First we examine the time invariant channel. We create a data segment representing a time invariant channel by repeating ten times the first snapshot of ARTM Flight 11 at time 18:53:38. The parameter based approach results in the scattering function and Doppler power spectrum of Figure 5.5 and the corresponding data based approach results in the plots of Figure 5.6. These estimates of Figure 5.5 are easily recognized as coming from a time-invariant channel [5,7] and they are extremely similar to the data based plots of Figure 5.6.

We consider Figure 5.5 first. The information is concentrated at a Doppler shift of zero and drops off either side directly to zero (-150 dB). In the delay axis, it is particularly simple to read: except at delays of $\tau_1 = 59.7$ ns and $\tau_2 = 200$ ns, there is no power in the signal. This corresponds to the parameterized values of the first and second non-LOS signal components. Because the data consists of ten repetitions of one snapshot, these values were repeatedly parameterized. Thus, these are the only peaks in the plot in addition to the peak at a delay of zero, corresponding to the LOS path. This describes Figure 5.6 quite well, though the levels differ somewhat. In Figure 5.6, the levels are somewhat lower and more distributed over several delay values. Though the signal level is 10 dB higher at delays of roughly ± 60 ns and ± 200 ns than at other levels, the distinction is not as crisp as in Figure 5.5. This points out a slight weakness in the 3-ray model. Rather than consisting of two crisp non-LOS paths, the signal appears to contain peaks at two delays and a very small diffuse power arriving at nearby delay values. That corresponds to the fact that the reflectors in the terrain are not single points, but rather somewhat larger, uneven surfaces. Still, the peaks are 10 dB stronger than the diffuse parts, so the model describes the signal quite well.

The Doppler power spectra of Figures 5.5 and 5.6 are indistinguishable. Each clearly suggests that the Doppler bandwidth is zero and the coherence time is infinite [5,7]. In this case then, the parameter based model contains basically all the salient information of the bulkier data set.

As a final example, we consider a rapidly changing channel. Figures 5.7 and 5.8 show striking similarities and further confirm the power of parameter based estimates. In each, the power levels drop unevenly to -25 dB as the Doppler shift moves from zero to $\pm 0.07 \text{ m}^{-1}$. Then the level increases at $\pm 0.08 \text{ m}^{-1}$. Over the window of our observation, both Doppler power spectra agree to within 5 dB and both indicate that there is a significant level of power over the whole range. This means that the Doppler bandwidth exceeds the range available to us to measure (6.7Hz) and the coherence time is shorter than the snapshot separation of our data [7].

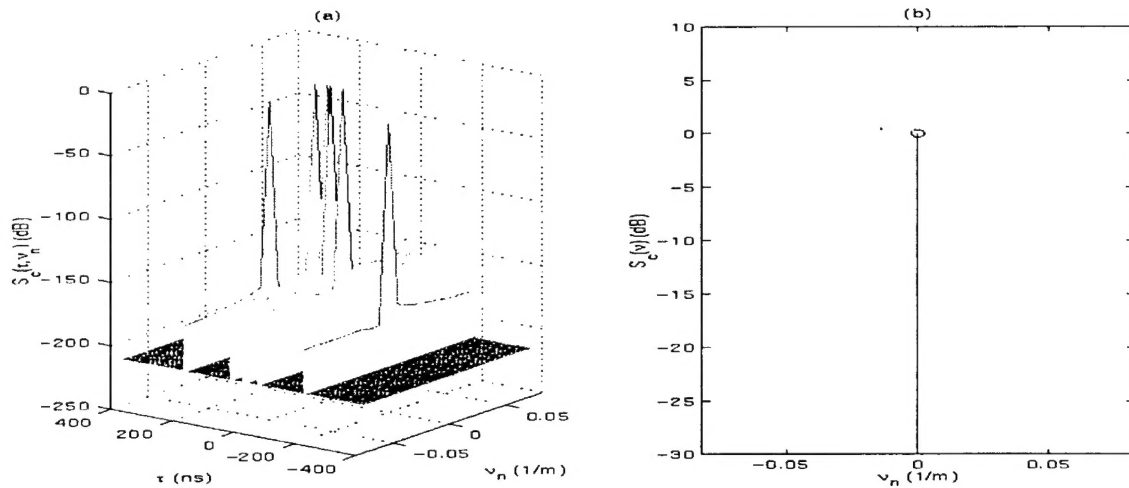


Figure 5.5: Parameter based estimates of (a) the scattering function $S_c(\tau, \nu_n)$ and (b) the Doppler power spectrum, $S_c(\nu_n)$ of a simulated time-invariant channel constructed by repeating ten times the first snapshot of ARTM Flight 11 at time 18:53:38 as diagrammed in Figure 5.2.

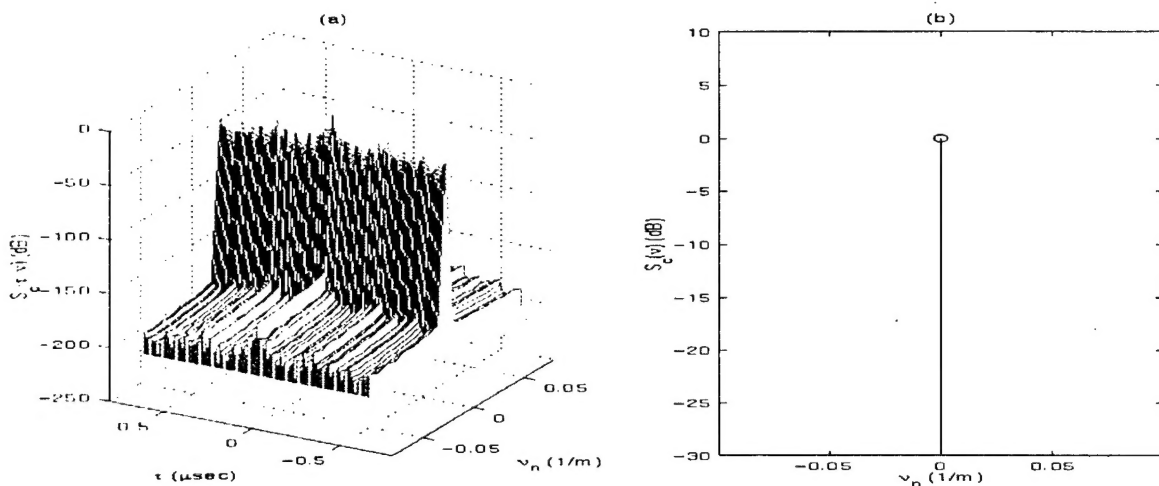


Figure 5.4: Data based estimates of (a) the scattering function, $S_c(\tau, \nu_n)$ and (b) the Doppler power spectrum, $S_c(\nu_n)$ of a simulated time-invariant channel consturcted by repeating ten times the first snapshot of ARTM Flight 11 at time 18:53:38 as diagrammed in Figure 5.1.

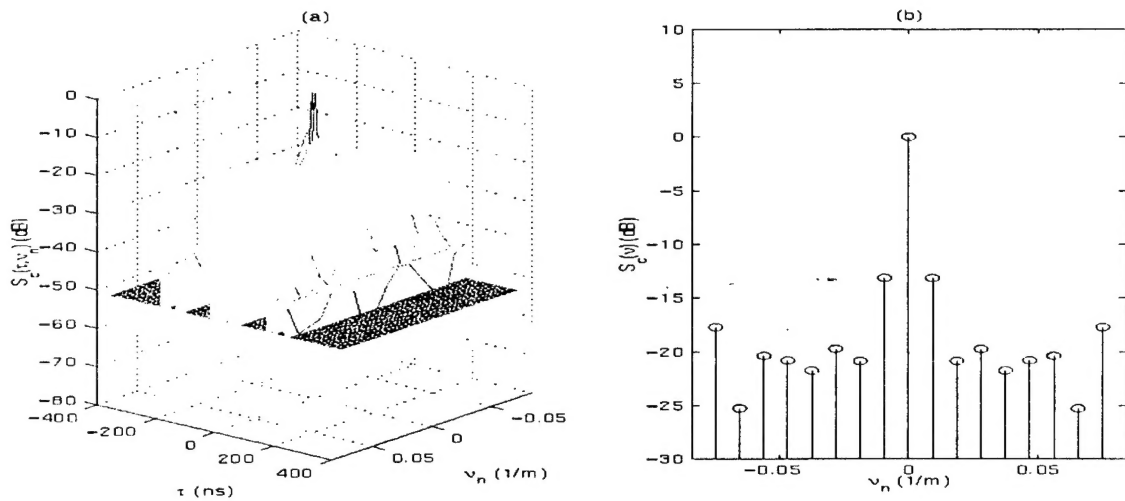


Figure 5.5: Parameter based estimates of (a) the scattering function, $S_c(\tau, v_n)$ and (b) the Doppler power spectrum, $S_c(v_n)$ of ARTM Flight 11 at 18:53:38 as diagrammed in Figure 5.2.

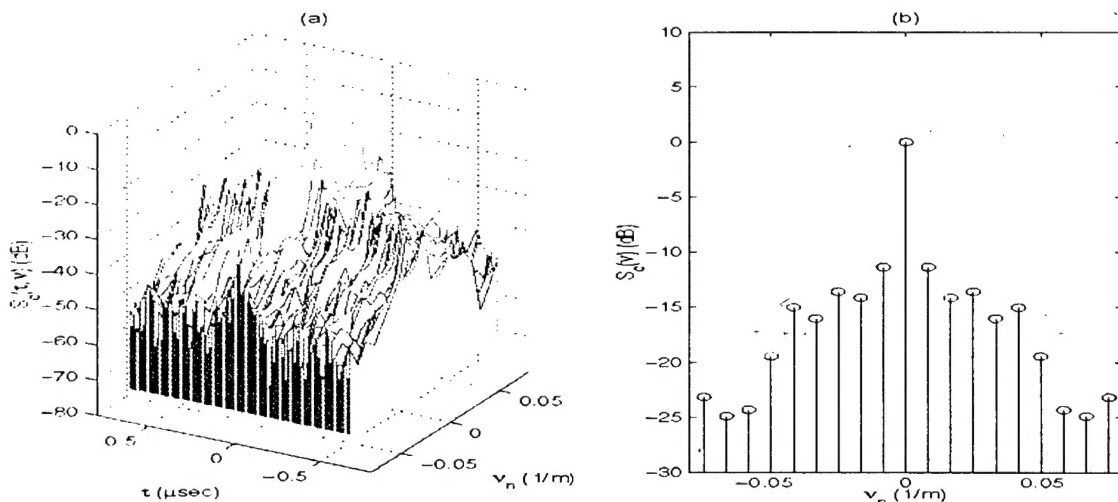


Figure 5.8: Parameter based estimates of (a) the scattering function, $S_c(\tau, v_n)$ and (b) the Doppler power spectrum, $S_c(v_n)$ of ARTM Flight 11 at 18:53:38 as diagrammed in Figure 5.2.

5.4 Results

We have found that a parameter based estimate of the scattering function has many advantages and few weaknesses relative to a purely data based estimate. For cases in which the channel changes very rapidly or is entirely constant, both the parameter based and data based estimates provide roughly the same information about the channel. Visually, they are very similar.

Further, derivative functions and values taken from the scattering function such as the Doppler power spectrum, Doppler bandwidth and coherence time are fairly similar for both approaches.

This agreement suggests that our model of the channel is a reliable one. Because the scattering function is a sophisticated reflection of the channel's time-dependent behavior, our results indicate that our modeling assumptions are good even as the channel changes over time. Thus, the telemetry channel of ARTM Flights 10 and 11 may be treated as a three-ray model which is wide-sense stationary, exhibits uncorrelated scattering, and is characterized by a uniformly distributed phase independent of the delay and magnitude distributions for each non-LOS path component.

The success of this model leads us toward a possible closed-form expression of the scattering function for the ARTM channel. We apparently have only sparse amounts of non-redundant information in the channel sounding data. A single LOS component and two non-LOS components constitute the bulk of our signal and are fairly adequate for describing the behavior of the channel at any instant. A description of the behavior of these sparse components very nearly describes the whole channel. This in principle is the final, unexplored branch in the diagram of Figures 5.1 and 5.2. An understanding of the 4-dimensional pdf of the magnitudes and delays, $(\Gamma_1, \tau_1, \Gamma_2, \tau_2)$ along with our understanding that the phase is independent and uniformly distributed would give us all we need to find a closed-form expression of the scattering function. This is a direction of current research but lies beyond the scope of this paper. At present, our parameter based estimate of the scattering function relies on measured data. Perhaps it will soon be possible to fully parameterize the problem and work independent of specific data sets in simulating the ARTM channel behavior.

6 REFERENCES

- [1] Rice, M., "ARTM Channel Sounding Results – An Investigation of Frequency Selective Fading on Aeronautical Telemetry Channels," in Proceedings of the International Telemetering Conference, volume 35, Las Vegas, Nevada, October 1999, pages 767-787.
- [2] Gagliardi, R., Satellite Communications, Van Nostrand Reinhold Co., New York, New York, 1984.
- [3] Rice, M., "Antenna Gain Pattern Effects on Multipath Interference in Aeronautical Telemetering," in Proceedings of the International Telemetering Conference, volume 33, Las Vegas, Nevada October 1997, pages 113-120.
- [4] Couch, L. W. II, Digital and Analog Communication Systems. Fifth Edition, Prentice-Hall, Upper Saddle River, NJ, 1997, pp. 167-168.
- [5] David Landon, "An analysis of Dynamic Behavior of the Aeronautical Telemetry Channel," Master's Thesis, Brigham Young University.
- [6] John G. Proakis, Digital Communications, McGraw Hill Companies, Inc., New Your, 1989, p. 461.

[7] Landon, David, "Doppler Bandwidth Characterization of ARTM Channel Sounding Data," Proceedings of the International Telemetering Conference, vol. 35, October 1999.

[8] Bello, Philip A., "Characterization of Randomly Time-Variant Linear Channels," IEEE Transactions on Communication Systems, vol. CS-11, pp. 360-392, 1963.